processes

MDPI

Article

Graphene Oxide as Valuable Additive for Improving ZnO Electrochemical Properties: Zn/xGO (x = 0, 0.1, and 0.5 wt.%) as Photoelectrocatalysts for Water Splitting and Electrochemical Sensor for Diclofenac

Ana Nastasić [1], Katarina Aleksić [2], Marija Kratovac [3], Ljiljana Veselinović [2], Ana Stanković [2], Marijana Kraljić Roković [4], Srečo Škapin [5], Valentin N. Ivanovski [1], Jelena Belošević-Čavor [1], Ana Umićević [1], Ivana Stojković Simatović [3] and Smilja Marković [2,*]

[1] "Vinča" Institute of Nuclear Sciences-National Institute of the Republic of Serbia, University of Belgrade, P.O. Box 522, 11001 Belgrade, Serbia; ana.nastasic@vin.bg.ac.rs (A.N.); valiva@vin.bg.ac.rs (V.N.I.); cjeca@vinca.rs (J.B.-Č.); umicev@vin.bg.ac.rs (A.U.)
[2] Institute of Technical Sciences of SASA, 11000 Belgrade, Serbia; katarina.aleksic@itn.sanu.ac.rs (K.A.); ljiljana.veselinovic@itn.sanu.ac.rs (L.V.); ana.stankovic@itn.sanu.ac.rs (A.S.)
[3] Faculty of Physical Chemistry, University of Belgrade, 11000 Belgrade, Serbia; marijakratovac20@gmail.com (M.K.); ivana@ffh.bg.ac.rs (I.S.S.)
[4] Department of Electrochemistry, Faculty of Chemical Engineering and Technology, University of Zagreb, 10000 Zagreb, Croatia; mkralj@fkit.unizg.hr
[5] Advanced Materials Department, "Jožef Stefan" Institute, Jamova Cesta 39, 1000 Ljubljana, Slovenia; sreco.skapin@ijs.si
* Correspondence: smilja.markovic@itn.sanu.ac.rs; Tel.: +381-11-2636-994

Abstract

Graphene oxide (GO) was employed as an additive to improve the electrochemical activity of zinc oxide (ZnO) used as both a photoelectrocatalyst for water splitting and an electrochemical sensor for detection of diclofenac. To comprehend the influence of a small amount of GO on the electrochemical activity of ZnO, a series of ZnO/*x*GO (x = 0, 0.1, and 0.5) particles was synthesized by microwave processing of $Zn(OH)_2$ precipitate in the presence of 0.1 and 0.5 wt.% of previously prepared GO. The phase composition and crystal structure ordering of ZnO/*x*GO particles were investigated by XRD and Raman spectroscopy. The optical properties were studied by UV–Vis DRS and PL spectroscopy. The particle morphology was inspected by FE–SEM while the textural properties were analyzed by the low-temperature nitrogen adsorption–desorption method. The (photo)electrocatalytic and electrochemical sensing activities were examined on the ZnO/r*x*GO modified glassy carbon electrodes (GCEs) prepared by in situ reduction of the ZnO/*x*GO modified GCEs for 120 s. The electro- and photoelectrocatalytic activity of ZnO/r*x*GO modified GCEs for water splitting was tested in dark conditions and after 60 min under illumination, respectively, employing linear sweep voltammetry in 0.1 M NaOH and 0.1 M H_2SO_4 as electrolytes. The electrochemical sensing activity of ZnO/r*x*GO modified GCEs was tested for detection of diclofenac in aqueous solution. The improvement in the electrochemical activity of ZnO was correlated with the added amount of GO, structural defects, and particle morphology.

Keywords: ZnO; graphene oxide; photoelectrocatalysts; electrochemical sensors; diclofenac

Academic Editor: Gustavo M. Morales

Received: 20 February 2026
Revised: 4 April 2026
Accepted: 21 April 2026
Published: 30 April 2026

https://doi.org/10.3390/pr14091453

1. Introduction

Contemporary society is facing parallel challenges related to the ever-growing demand for energy and the increasing severity of environmental pollution, with water contamination holding a particularly important position. Population growth, inadequate management of water and energy resources, climate change, and increased industrial activity have made clean water and zero-carbon energy critical global resources [1,2]. In this context, the development of multifunctional materials is drawing more attention from researchers, as they enable simultaneous addressing of issues associated with sustainable energy production and the efficient removal/detection of pollutants in aquatic systems [3].

One promising approach to fulfill the global energy demand is photoelectrochemical water splitting for producing green hydrogen, an energy carrier with high energy density and zero emission of harmful byproducts [4–6]. It involves the splitting of water into hydrogen and oxygen through two half-reactions: the hydrogen evolution reaction (HER) and the oxygen evolution reaction (OER), which are driven by absorbed solar energy using photoelectrocatalysts [7–9]. Pt/C is recognized as the most efficient electrocatalyst for HER, while IrO_2 and RuO_2 are the benchmark catalysts for OER. However, their scantiness, high price, and poor chemical stability motivate the search for alternative HER/OER electrocatalysts. Among these, wide-bandgap metal oxides, such as ZnO and TiO_2, have attracted particular attention due to their chemical stability, low price, and suitability for photoelectrochemical applications [10–13].

In addition to energy-related considerations, growing concern about drinking, surface, and groundwater quality has accelerated research in the field of electrochemical pollutant detection. Electrochemical sensors offer high sensitivity and selectivity, and rapid, facile, and low-priced analysis, which make them suitable for on-site monitoring of chemical and biological pollutants, and their degradation products in aqueous matrices [14]. An interest in on-site analyte detection inspired many electrochemical investigations to be focused on pesticide and fertilizer sensing, especially because their residues are frequently present in water sources and could deteriorate human health by being cytotoxic, carcinogenic, and mutagenic [15–17]. Due to detrimental effects on human health and the environment, there is also growing interest in developing electrochemical sensors for detection of per- and polyfluoroalkyl substances (PFASs, known as "forever chemicals") [18–20]. Until now, electrochemical sensors have been tested for quantification of pharmaceutical components in herbal medicine; this is especially important since some, e.g., flavonoid compounds, often exhibit good antioxidant, anti-inflammatory, and anticancer properties, offering great benefits to human health, while excessive intake may cause many adverse heathy risks such as convulsions, dizziness, and coma [21]. It has been shown that electrochemical sensors can be successfully used for monitoring heavy metal ions which are particularly hazardous due to their high toxicity, environmental persistence, and bioaccumulation [22,23]. The development of electrochemical sensors for dyes has been triggered by the necessity for quick and effective quantifying of some synthetic azo colors utilized in food production, especially since they may be extremely poisonous, resulting in DNA alterations [24]. A significant part of the investigations is devoted to the development of biosensors for detection of infectious diseases, cancer cells [25–27], etc. Among present-day pollutants, pharmaceuticals have also been recognized as particularly concerning due to their widespread use, environmental persistence, as well as potential unpredictable and long-term effects on ecosystems and human health [28]. Non-steroidal anti-inflammatory drugs, such as diclofenac, are widely used and frequently detected in natural waters, thus requiring the development of reliable and efficient detection and quantification methods [28–30].

Considering the increasing demand for zero-carbon energy sources and effective water pollution controls, further research should therefore focus on the development of novel, stable, and efficient multifunctional materials that could integrate catalytic activity for HER and OER with electrochemical pollutant detection capabilities. To the best of the authors' knowledge, no material has been reported in the literature that has been investigated for both HER/OER photoelectrocatalysis and diclofenac detection in the water environment. This gap in the literature highlights a potential research opportunity for developing multifunctional catalysts for energy and environmental monitoring applications. In this respect, graphene oxide represents an attractive material due to its structural, electronic, and surface properties, as well as its ability to form composites with transition metal oxides, such as ZnO, making it a viable framework for the development of multifunctional materials in photoelectrochemical and electrochemical applications [1,31].

Transition metal oxides have been extensively investigated in photocatalysis and energy-related applications due to their semiconducting properties and ability to easily change oxidation states [3]. Among transition metal oxides, ZnO is one of the most studied n-type semiconductors owing to its wide band gap, chemical stability, low cost, biocompatibility, non-toxicity, and well-established applications in electronics and optical devices [3,5,32]. Its ability to form various nanostructures (such as nanowires, nanorods, nanoplates, etc.), which provides a high surface-to-volume ratio, and enhanced reactivity make it a promising material for photoelectrocatalysis, as well as environmental applications like pollutant detection [3,32]. However, despite research efforts, the practical performance of ZnO is limited by low electrical conductivity, high charge recombination rates, and a tendency toward photodegradation under UV irradiation [3]. Consequently, composite formation with other functional materials is commonly employed to improve charge transfer, stability, and overall catalytic performance.

Graphene oxide (GO) is widely used as a material to improve charge transfer, particularly in composites and hybrid materials for energy, catalytic, and sensing applications. GO is a two-dimensional carbon material featuring rich oxygen-containing functional groups (such as hydroxyl, epoxy, and carboxyl groups) distributed across its basal plane and edges [33]. It possesses a large specific surface area (SSA), excellent thermal and mechanical stability, and tunable electronic properties, which make it a convenient material for various applications [1,22,34,35]. While GO itself exhibits limited intrinsic photocatalytic activity, it has been successfully combined with semiconductor oxides, such as TiO_2 and ZnO, to enhance photocatalytic performance [1]. Moreover, its large SSA contributes to better exposure of active sites, which is beneficial for both water splitting and sensing applications [4,36]. However, the high sheet resistance of pristine GO and potential structural defects can limit its conductivity, which is typically addressed by reduction and/or composite formation [1]. Owing to these versatile characteristics, GO could serve as a robust platform for designing multifunctional materials.

Having in mind previously published results about GO nanocomposites with transition metal oxides, which demonstrated improved catalytic, photocatalytic, and sensing properties [31,37–39], we were intrigued by the possibility of developing a cost-effective and green procedure for processing ZnO/GO composites, where GO can be employed to control the morphology, bulk and surface defect states, and photoresponse of ZnO nanocrystals (where the migration efficiency of photo-induced electrons can be promoted, while electron–hole recombination in carrier transfer processes can be inhibited). Thus, the purpose of this research was to improve the electrochemical properties of ZnO by employing a small amount of graphene oxide, i.e., 0.1 and 0.5 wt.% (relative to $ZnCl_2$). As an innovation compared to up-to-date published procedures for ZnO/GO composite processing, GO particles were dispersed in $ZnCl_2$ solution before the process of $Zn(OH)_2$ precipitation by NaOH. In this way, GO particles served as seeds for $Zn(OH)_2$ precipitation, influencing further ZnO particle crystallization in the MW field. We examined how the rela-

https://doi.org/10.3390/pr14091453

tive content of GO affects phase composition, crystal structure ordering—especially surface and bulk oxygen vacancies—optical properties, morphology, and the textural properties of prepared ZnO/xGO (x = 0, 0.1, and 0.5) particles. To comprehend the influence of GO on the functional properties of ZnO/xGO particles, we estimated their (1) photoelectrocatalytic activity towards HER and OER, in both acidic and alkaline electrolytes, and (2) electrochemical performance for detection of diclofenac in a neutral aqueous electrolyte. Both sets of experiments were completed on GCEs modified by ZnO/xGO after in situ reduction for 60 s, twice in a row. An improvement in the functional properties of ZnO/xGO compared to bare ZnO was correlated with physicochemical properties influenced by the addition of GO, highlighting the role of charge transfer and oxygen vacancies.

2. Materials and Methods

2.1. Materials

Zinc chloride ($ZnCl_2$, >99.5%, Lach-Ner, Neratovice, Czech Republic), sodium hydroxide (NaOH, >98%, CARLO ERBA Reagents, Cornerado (MI), Italy), and graphene oxide (GO, prepared in our laboratory according to the procedure described in a previous publication [40]) were used in synthesis procedures. Distilled water and absolute ethanol (Zorka, Šabac, Serbia) were used as the solvents for initial rinsing to remove salt residues and the final rinsing of the synthesized powders, respectively.

2.2. Synthesis of ZnO/xGO (x = 0, 0.1, and 0.5) Particles

The ZnO/xGO (x = 0, 0.1, and 0.5) particles were synthesized using the microwave processing of a precipitate method. For the synthesis of zinc oxide (x = 0), 0.8977 g of $ZnCl_2$ was dissolved in 100 mL of distilled water under magnetic stirring. After 5 min, 20 mL of 1.75 M NaOH solution was added dropwise, resulting in the formation of an off-white precipitate. The suspension was stirred at 50 °C for 90 min. The precipitate was then transferred into a microwave oven (2.45 GHz, 130 W) and treated for 5 min, after which it was cooled to room temperature under ambient conditions. The sample was collected by centrifugation at 7000 rpm for 5 min at 22 °C and rinsed five times with distilled water and five times with ethanol. The obtained particles were dried at 80 °C for 24 h and powdered in an agate mortar. For the synthesis of ZnO/xGO particles with x = 0.1 and 0.5, a selected volume of graphene oxide dispersion (8.5 mg mL^{-1}) was added to 100 mL of distilled water to obtain graphene oxide contents of 0.1 wt% and 0.5 wt% relative to $ZnCl_2$. After 5 min of stirring, 0.8977 g of $ZnCl_2$ was added, and the procedure was continued as described for zinc oxide.

The synthesized particles were denoted as ZnO, ZnO/0.1GO, and ZnO/0.5GO, where the numbers 0.1 and 0.5 indicate the wt.% of GO used for the synthesis relative to the mass of $ZnCl_2$.

2.3. Characterization of ZnO/xGO (x = 0, 0.1, and 0.5) Particles

X-ray diffraction (XRD) data were collected on a Philips PW 1050 diffractometer with $CuK\alpha_{1,2}$ (λ = 1.54178 Å) Ni-filtrated radiation, operating at 40 kV and 20 mA. The XRD scans were conducted over the angular range from 10 to 70° 2θ, with a step size of 0.05° and a dwell time of 5 s per step. The crystal phases were identified using Match!3 database software (Version 3.5) [41], with reference to the Crystallography Open Database (COD) patterns [42]. The XRD microstructural analysis was performed by the Rietveld refinement method using the FullProf computing program [43,44]. In order to subtract instrumental broadening, the XRD pattern of a LaB_6 standard was fitted. μ-Raman spectra were recorded on a Thermo Scientific DXR Raman microscope (Waltham, MA, USA), equipped with an optical microscope and a CCD detector, using the 532 nm diode-pumped solid-state highbrightness laser as the excitation source, at a power of 2 mW. The spectra were recorded in the frequency interval of 50–3500 cm^{-1} with a resolution of 4 cm^{-1}, exposition time 10 s, number of expositions 10. Photoluminescence (PL) spectra were recorded in the 350–700 nm range, using a Horiba Jobin Yvon Fluorolog FL3–22 spectrofluorometer equipped with a xenon (Xe) lamp as the excitation source. Excitation was performed at a wavelength of 280 nm. The UV–Vis DRS was measured in the range from 800 to 200 nm using an Agilent Cary 5000 spectrophotometer equipped with a diffuse reflectance accessory. A commercial PTFE standard was used for baseline correction. The morphology and particle size of the prepared samples were examined using field-emission scanning electron microscopy (FE-SEM, Ultra Plus Carl Zeiss, Jena, Germany), before analysis samples were dispersed in water for 5 min and immediately filtered through a polycarbonate membrane. The membrane was fixed on carbon tape on an aluminum stub, and to ensure good electrical conductivity during FE-SEM investigation, the samples were carbon coated using a PECS (Gatan GmbH, Model 682, Munich, Germany). The specific surface area (SSA) and the total pore volume were determined based on a N_2 adsorption–desorption isotherm at −195.8 °C using an ASAP 2020 (Micromeritics Instrument Corporation, Norcross, GA, USA). Prior to analysis samples were degassed under reduced pressure at 120 °C for 10 h. The SSA was calculated according to the Brunauer–Emmett–Teller (BET) method from the linear part of the N_2 adsorption isotherm. The total pore volume (V_{total}) was estimated from the adsorbed amount at a relative pressure $p/p^0 = 0.998$.

2.4. Electrochemical Measurements

All electrochemical measurements were accomplished using an Ivium VertexOne potentiostat/galvanostat in a standard three-electrode setup consisting of the modified glassy carbon electrode (GCE) as a working electrode, a platinum (Pt) foil as the counter electrode, and a saturated calomel electrode (SCE) as the reference electrode. Prior to each electrochemical measurement, in situ electrochemical reduction of GO of each ZnO/GO modified electrode was performed by chronoamperometry in 0.1 M KCl ($E = -1.4$ V vs. SCE) for 1 min, repeated twice. (In the text, the reduced electrodes are denoted as ZnO/rxGO.) Following the reduction step, ZnO/r0.1GO and ZnO/r0.5GO were subjected to electrochemical evaluation, together with the ZnO.

For photoelectrocatalytic activities of the ZnO particles, the working electrodes were prepared by coating 5 μL of catalytic ink onto a glassy carbon, followed by drying under an IR lamp for 60 s to enable solvent evaporation. The catalytic inks were prepared by dispersing 10 mg of ZnO/xGO particles into a mixture of 10 μL of 5% Nafion solution (Sigma-Aldrich, Saint Louis, MO 63103, USA), 50 μL of water, and 50 μL of ethanol in an ultrasonic bath for 1 h.

Both acidic (0.1 M H_2SO_4) and alkaline (0.1 M NaOH) electrolytes were used for photoelectrocatalytic measurements using linear sweep voltammetry (LSV) at a scan rate of 20 mV s^{-1}. For OER measurements, LSV was performed in the potential range of 0.2 to 1.9 V vs. SCE in both media. For HER measurements, the applied potential ranges were 0.2 to −1.9 V vs. SCE in alkaline medium and 0.2 to −1.0 V vs. SCE in acidic medium.

All potentials were measured against the SCE and converted to a reversible hydrogen electrode (RHE) scale using the Nernst Equation (1) [45]:

$$E_{RHE} = E_{SCE} + 0.059\,pH + 0.244 \tag{1}$$

The measurements were accomplished in the dark and under illumination. For the illuminated measurements, the electrodes were exposed to light produced by Spectromaster 250 W 6400 K CFL bulb (wavelength 400–700 nm, with peak around 450–500 nm) at an irradiance of 100 mW cm^{-2} (the light intensity was measured by a PeakTech 5165 Digital-

Lux-Meter, Ahrensburg, Germany) for 60 min. The distance between the electrochemical cell and the light source was 10 cm.

The inks for electrochemical detection of diclofenac were prepared by combining 10 mg of ZnO/*x*GO particles, 1.5 mg of a Vulcan carbon additive (CABOT VULCAN Carbon Black XC72R), 40 µL of a 5% Nafion solution, 225 µL of distilled water, and 225 µL of ethanol. The resulting mixture was briefly vortexed and then ultrasonically treated for 1 h to ensure homogenization. The prepared ink was deposited as a thin film onto a GCE, and then dried under an infrared lamp (Avide, 250 W). This procedure resulted in modified GCEs.

Cyclic voltammetry (CV) was employed to evaluate materials' electrochemically active surface area (EASA) and heterogeneous electron transfer rate constant (k^0). The voltammograms were recorded within a potential window of −0.4 to 1.0 V vs. SCE, using a potential step of 2 mV and a polarization rate of 20 mV s^{-1}. Measurements were carried out in a 5 mM $K_4[Fe(CN)_6]$ solution prepared in 0.1 M KCl, which served as the supporting electrolyte. EASA and k^0 values were calculated based on the Randles–Ševčik equation and Nicholson's method, respectively, following the previously reported methodology [46].

Overpotential (η) was determined as the difference between the applied potential at a fixed current density and the thermodynamic equilibrium potential of the corresponding reaction. Overpotential at 10 mA cm^{-2} (η_{10}) was calculated for HER and OER in both acidic and alkaline media using Equations (2) and (3), respectively [45]:

$$\eta_{OER} = E_{RHE} - 1.23\ V \tag{2}$$

$$\eta_{HER} = E_{RHE} - 0\ V \tag{3}$$

The turnover frequency (TOF) was calculated for all samples under both dark and illuminated conditions in alkaline and acidic electrolytes, using Equation (4) [47]:

$$TOF = (j \cdot N_A)/(n \cdot F \cdot \Gamma) \tag{4}$$

where j is the current density (A cm^{-2}), NA is the Avogadro number, n is the number of electrons transferred (2 for HER, 4 for OER), F is the Faraday constant (96,485 C mol^{-1}), and Γ is the surface concentration of active sites (sites cm^{-2}) determined using Equation (5) [48]:

$$\Gamma = EASA/A_{geom} \cdot \Gamma_{ZnObalk} \tag{5}$$

where EASA is electrochemically active surface area, A_{geom} = 0.3 cm^2 and $\Gamma_{ZnObalk}$ is $0.05 \cdot 10^{15}$ sites cm^{-2} [49]. The current density values used for TOF calculation were determined from the LSV curves at the fixed potentials: −0.25 V vs. RHE for HER in acidic medium, −0.30 V vs. RHE for HER in alkaline medium, and 1.73 V vs. RHE for OER in both acidic and alkaline media.

Linear sweep voltammograms (LSVs) were recorded to investigate the electroanalytical response of the materials in the potential range from 0.2 V to 0.8 V vs. SCE, using a potential step of 2 mV and at a scan rate of 20 mV s^{-1}. Electroanalytical measurements were performed in 0.1 M phosphate buffer (pH~7). Diclofenac (Diclofenac HF, injection solution, 75 mg/3 mL, Hemofarm STADA, Vršac, Serbia) was added to the electrolyte in successive 1 µL additions, with the solution being stirred for 5 min after each addition, i.e., prior to electrochemical measurements. The limit of detection (LOD) and the limit of quantification (LOQ) were determined according to Equations (6) and (7), where σ represents the standard deviation of y-intercept of the calibration plot and b denotes the slope of the same calibration line [50]. Additionally, b represents the sensitivity of the analytical method.

$$\mathrm{LOD} = \frac{3\sigma}{b} \tag{6}$$

$$\mathrm{LOQ} = \frac{10\sigma}{b} \tag{7}$$

2.5. Computational Procedure

To comprehend the electrochemical activity of the ZnO/xGO systems, density functional theory (DFT)-based calculations were performed utilizing the projector augmented wave (PAW) method within the Vienna ab initio simulation package (VASP) [51,52]. In the performed calculations, the surfaces were modeled as periodically repeated slabs consisting of several atomic layers and separated by a vacuum region. For the ZnO (000-1) surface of 16 layers, the top 8 layers were allowed to relax pending the Hellmann–Feynman forces being reduced below 0.02 eV/Å, whereas the rest of the layers were held fixed, representing the bulk crystal. For the graphene supercell of 128 carbon atoms, the borderline atoms were kept fixed. The Perdew–Burke–Ernzerhof (PBE) generalized gradient approximation (GGA) [53] was used for the exchange-correlation functional and the plane-wave basis set cutoff of 500 eV. Self-Consistent Field (SCF) energy convergence threshold was 10^{-6} eV. Due to a large number of atoms and faster energy convergence, the k-point mash with only the gamma point of the Brillouin zone was chosen. For the graphene lattice constant, the literature value of 2.46 Å was used [54]. After the surface optimization, the molecule of diclofenac was put above the surface of both ZnO and graphene and the equilibrium adsorption configuration, as well as the adsorption energy, were calculated. Bader's atoms-in-molecules theory [55] was used to calculate the charge redistribution between the atoms in the investigated systems. For the Bader's charges calculations, the energy convergence criterion was set to 10^{-8} eV. The bond orders and the overlap populations between orbitals were calculated by the DDEC6 method for atomic population analysis in periodic and non-periodic materials implemented in the Chargemol program [56].

Adsorption binding energy of a molecule to the surface was calculated using Equation (8) [57]:

$$E_{ads} = E_{complex} - E_{surface} - E_{molecule} \tag{8}$$

where $E_{complex}$ is the energy of the optimized complex consisting of the ZnO surface (or graphene) and diclofenac molecule on top of it, $E_{surface}$ is the energy of the ideal ZnO surface (or graphene), and $E_{molecule}$ is the energy of the diclofenac molecule.

3. Results and Discussion

3.1. Physicochemical Characteristics of ZnO/xGO Particles

The influence of GO particles on the phase composition and crystal structure ordering of ZnO/xGO particles was investigated using XRD and Raman spectroscopy analyses; the diffraction patterns and Raman spectra are presented in Figure 1a,b. The diffraction patterns indicate highly crystalline ZnO particles with a Wurtzite-type hexagonal symmetry ($P6_3mc$ space group; COD no. 96-230-0113); Figure 1a [42]. The XRD patterns show that ZnO/0.1GO and ZnO/0.5GO possess the same phase compositions as bare ZnO, which is expected since a small amount of GO used for the synthesis cannot be detected by X-ray diffraction. However, structural analysis performed by the Rietveld refinement full pattern method confirm that even a small amount of GO influenced crystal growth, particularly the unit cell parameters, crystallite size (calculated for three specific crystallographic directions [100], [002] and [101], and average), average strain and crystallinity; the calculated values are listed in Table 1. The unit cell parameters calculated for bare ZnO particles were found to be $a = b = 3.2497(3)$ Å, $c = 5.2103(6)$ Å, $V = 47.643(2)$ Å^3, matching the standard COD parameters for the hexagonal ZnO crystals with a Wurtzite-type structure (COD no. 96-230-0113). The crystallite sizes in three specific crystallographic directions, [100], [002], and [101], were found to be 15.2, 14 and 13.3 nm, respectively. As can be noticed from data listed in Table 1, the presence of GO in ZnO/0.1GO influenced the lattice parameters; the unit cell parameters slightly decreased while the crystallite size in [100], [002], and [101] directions increased to 26.0, 23.4, and 22.2, respectively. A further increase in the GO amount in ZnO/0.5GO provoked slight changes in both unite cell parameters and the crystallite size. Variation in the crystallite sizes and the crystallinity degree in ZnO/*x*GO compared with the bare ZnO can be explained by the fact that a small amount of GO acts as a substrate which promotes the crystallization of ZnO [58,59]. However, an increase in GO concentration in a mixture with ZnO induces a chemical reaction between the functional GO groups which contain oxygen and ZnO, acting subsequently as an inhibitor of crystallite growth [60]. The calculated average lattice strain varied from 6.1×10^{-3} for the bare ZnO via 3.9×10^{-3} for ZnO/0.1GO to 5.5×10^{-3} for ZnO/0.1GO, implying the largest concentration of lattice defects in ZnO and the most ordered crystal structure of ZnO/0.1GO [61]. In addition, the calculated polarity values $I_{(002)}/I_{(100)}$ were found to be 1.045, 1.026, and 1.045 for ZnO, ZnO/0.1GO, and ZnO/0.5GO, respectively, indicating an almost isotropic nano-crystallite growth [10]. The values of the polarity $I_{(002)}/I_{(100)}$ around 1, for all examined ZnO/*x*GO particles, indicate a well-developed polar (0001) plane (inset in Figure 1a) with a hexagonal platelike morphology, implying that synthesized nanoparticles could be very electrochemically active. Considering the polarity and the calculated crystallite size in [100], [002], and [101] directions, a more profound electrochemical activity can be expected for ZnO/0.1GO which has the most developed crystallites.

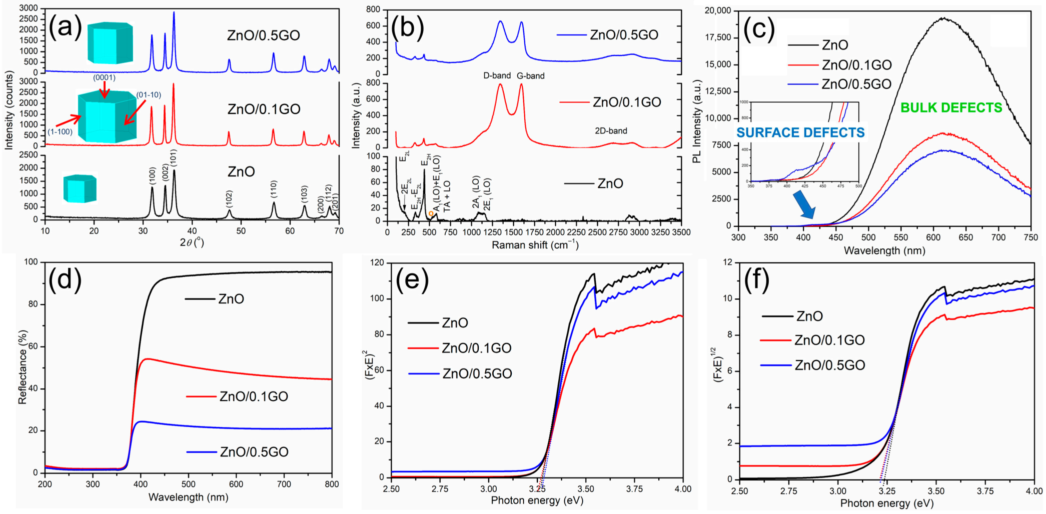

Figure 1. (**a**) XRD patterns with scheme of ZnO crystallites, (**b**) Raman, (**c**) PL, and (**d**) UV-Vis DRS spectra, and Kubelka–Munk plots for (**e**) direct, and (**f**) indirect bandgap of ZnO/xGO particles.

Table 1. Unit cell parameters (with standard deviations), crystallite sizes (in specific crystallographic directions and on average), average strain, polarity, crystallinity degree and textural (SSA and total volume of pores) properties of ZnO/*x*GO particles.

Sample Notation	Unit Cell Parameters			Crystallite Sizes, D (nm)				Average Strain	Polarity *	Crystallinity Degree (%)	SSA ** (m^2/g)	Vtot *** (cm^3/g)
	a = b (Å)	c (Å)	V (Å^3)	D_{100}	D_{002}	D_{101}	D_{av}	ε	I(002)/I(100)	Xc		
ZnO	3.2497 (3)	5.2103 (6)	47.643 (2)	15.2	14.0	13.3	14.5	6.1×10^{-3}	1.045	70	35	0.298
ZnO/0.1GO	3.2487 (7)	5.2042 (2)	47.568 (3)	26.0	23.4	22.2	28.6	3.9×10^{-3}	1.026	71	34	0.348
ZnO/0.5GO	3.2494 (4)	5.2054 (8)	47.597 (3)	20.5	18.3	17.1	17.2	5.5×10^{-3}	1.045	76	35	0.353

* Calculated from XRD intensity for (002) and (100) planes. ** Standard, $p/p^0 = 0.05$–0.25. *** at $p/p^0 = 0.99$.

Since XRD did not confirm the presence of GO in ZnO/*x*GO particles, we used Raman spectroscopy as a powerful tool for inspecting the presence of a small amount of GO in composites; Raman spectra are presented in Figure 1b. All bands in the Raman spectrum of bare ZnO are distinctive for the Wurtzite crystal structure [10]. The most intense peak at 98 cm^{-1}, labeled as E_{2L}, is due to vibrations of the zinc sublattice in ZnO [10,62,63]. The shoulder at 200 cm^{-1}, a sharp peak at 333 cm^{-1} and the weak shoulder near 380 cm^{-1} are assigned to the second-order phonon mode 2E_{2L}, the multi phonon mode E_{2H}–E_{2L}, and to A_1 (TO) vibrations, respectively. The weak shoulder at 410 cm^{-1} corresponds to the E_1 (TO) mode. The existence of E_1 (TO) vibrational mode indicates the growth of ZnO crystallites in a direction different than the *c*-axis typical of ZnO particles [10]; this is in agreement with the almost isotropic crystallite geometry estimated from the XRD data for the [100], [002], and [101] crystallographic directions (Table 1). The peak at 434 cm^{-1} is due to the E_{2H} mode and it is assigned to oxygen vibrations [64]. The asymmetry of the E_{2H} peak points to lattice disorder while its intensity indicates crystallinity; thus, a high intensity of the E_{2H} peak indicates a good crystallinity of ZnO particles which is in accordance with the crystallinity of about 70% calculated from the XRD data (Table 1) [65,66]. A wide band in the 510−740 cm^{-1} region consists of two peaks; the one at 570 cm^{-1} represents A_1 (LO) and E_1 (LO) modes, whereas the other, at 635 cm^{-1}, represents a combination of acoustic and optical modes (TA + LO). The A_1 (LO) mode is associated with bulk defects such as oxygen vacancies, zinc interstitials or defect complexes containing both [64]. It has been shown that the presence of defects strongly influences these modes, especially E_1 (LO) [66]. The relatively high intensity of the A_1 (LO) + E_1 (LO) modes in the Raman spectrum of the ZnO sample, Figure 1b, points to a relatively large amount of oxygen vacancies and zinc interstitials as intrinsic bulk defects. As we previously reported, these bulk defects were provoked by fast crystallization induced by microwave irradiation [10,63]. A weak peak at 483 cm^{-1} (marked with an orange circle) is attributed to the interfacial surface phonon mode 2LA [64]. The wide band in the wavenumber region 1090–1150 cm^{-1} is attributed to the optical overtone 2LO, explicitly to 2A_1 (LO) and 2E_1 (LO). The Raman spectra of ZnO/*x*GO look very similar, with bands typical for ZnO appearing in the 100 to 750 cm^{-1} spectral range and two intense bands centered near 1340 and 1595 cm^{-1}, denoted as the D- and G-band, respectively [67]. The D- and G-bands confirm the presence of GO in ZnO/*x*GO particles, where the D-band is related to a structural disorder in graphene, whereas the G-band is assigned to the sp^2 hybridized carbon atoms (C=C stretching), confirming the presence of carbon in the materials [67]. In the spectrum of ZnO/0.1GO the D- and G-bands are centered at 1341 and 1593 cm^{-1}, respectively, while in the spectrum of ZnO/0.5GO the bands are negligibly shifted to 1343 and 1594 cm^{-1}. We calculated the intensity ratio of the D- and G-bands as a useful indicator of the structural defects in graphitic materials [68]. The obtained values for I_D/I_G of 1.004 and 1.01 for ZnO/0.1GO and ZnO/0.5GO, respectively, confirm an almost identical concentration of structural defects in GO as a compositional part of ZnO/*x*GO.

The type and relative number of defects in the crystal structure of the ZnO/*x*GO particles, especially their dependence on the GO amount, were studied by employing photoluminescence (PL) spectroscopy. PL spectra of the ZnO/*x*GO particles, displayed in Figure 1c, have the same shape but with different intensities depending on the amount of GO. A broad emission band of high intensity centered at approximately 630 nm is associated with bulk defects, while the low-intensity band observed near 420 nm indicates a negligible amount of surface defects, inset in Figure 1c [10,63]. PL spectra indicate that even a small amount of GO (0.1 wt.%) added to $ZnCl_2$ solution before the precipitation procedure leads to a significant reduction in bulk defects in the ZnO crystal structure without an impact on surface defects. An additional increase in the GO amount (to 0.5 wt.%) further decreases the number of bulk defects in the ZnO crystal structure with a slight increase in surface defects. These results imply that ZnO/0.5GO possesses the most ordered crystal structure, which is in accordance with the highest crystallinity (76%) calculated from XRD data.

To investigate the influence of the GO amount on the optical properties of the ZnO/xGO particles, UV-Vis DRS was recorded. UV−Vis DRS plots show characteristic reflectance curves with the adsorption edge near 380 nm but with significantly different absorption capacity, Figure 1d. As can be seen, ZnO particles reflect about 93% of visible light, i.e., they absorb only 7%; ZnO/0.1GO absorbs between 45 and 55% of VIS in the range from 380 to 780 nm; while ZnO/0.5GO absorbs about 75%. As is known, GO exhibits strong absorption in the UV spectral region, with a peak at 230 nm and a weak absorption tail that extends up to 400 nm; thus, the significant enhancement in the visible light absorption of ZnO/xGO particles cannot be attributed to the simple presence of GO particles. The different absorption capacity in the visible spectral region could be attributed to different morphologies of ZnO particles (see Figure 2). As we previously stated, particles with a larger diameter or thickness have an enhanced absorption capacity due to a longer optical path for light transport, while surface defects can additionally enhance visible light absorption [63]. To estimate direct and indirect band gap energies (E_{bg}) of ZnO/xGO particles, we employed the Kubelka–Munk method [63]. Tauc plots were constructed by plotting $[F(R) \times E]^2$ and $[F(R) \times E]^{1/2}$ vs. photon energy E (eV), and the band gap energies were estimated by extrapolation of the linear part of the curves to $[F(R) \times E]^2$, i.e., $[F(R) \times E]^{1/2}$ to 0, Figure 1e,f. The estimated values for the direct band gaps were between 3.26 and 3.28 eV. The estimated values for the indirect bandgaps were 3.21 eV for all examined samples. Thus, GO in ZnO/xGO particles caused a negligible shift in the band gap energy toward the visible light region. The fact that, even after the introduction of GO to the ZnO, the band gap energy of ZnO/xGO is negligibly adjusted can be explained by the XRD results, which confirmed that ZnO particles retain the original Wurtzite structure within the composite, thus keeping their intrinsic band gap.

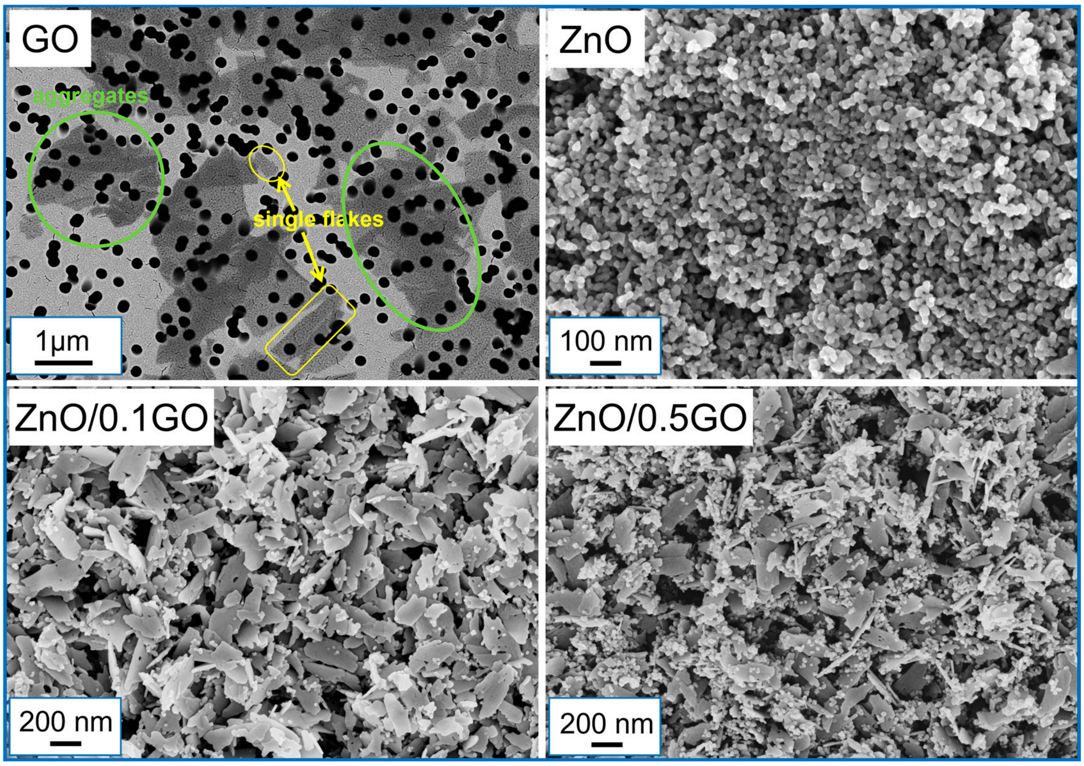

Figure 2. FE-SEM micrographs of graphene oxide (GO) flakes on a filter membrane, taken at 2.0 kV, and ZnO/xGO particles taken at 3 kV.

The presented results imply that the amount of GO in ZnO/*x*GO particles has no direct influence on structural and optical characteristics but an indirect one by influencing crystallization and particle growth. Here, particle size influenced the capacity of visible light absorption even without affecting the band gap energy.

Figure 2 shows the FE-SEM micrograph of graphene oxide (GO) flakes on a filter membrane, taken at a 2.0 kV voltage. Graphene oxide flakes, prepared in our laboratory according to the previously published procedure [40], are of sizes up to approximately 1 µm. Aggregates, which can be observed on the filter membrane, are due to the filtration procedure. FE-SEM images of ZnO confirm that under the applied experimental conditions, nearly spherical, monodisperse nanostructured particles with an estimated average size of 30 nm are formed. The addition of 0.1 wt% of GO to the initial $ZnCl_2$ reagent mixture before precipitation with NaOH resulted in the formation of platelike ZnO particles alongside nanosized, nearly spherical particles with similar morphology to those observed in the system without GO. The lateral size of the irregularly shaped platelets is estimated to be up to 500 nm, with a thickness of up to 30 nm in both samples. The estimated proportion of platelike particles in the sample containing 0.1 wt. % of GO is approximately 90%, while in the sample with 0.5 wt.% of GO the proportion of these particles is slightly lower, at approximately 80%.

FE-SEM analysis of the composite morphology confirms that even a small amount of GO, added to the initial $ZnCl_2$ reagent solution before starting precipitation with NaOH, influences the growth of $Zn(OH)_2$ particles on GO as seeds, which further impacts the crystallization in the MW field. Having in mind the results of the FE-SEM analysis together with XRD and UV-Vis DRS, we suppose that ZnO nanoparticles are formed on the surface of the GO sheets rather than being incorporated within the crystal lattice.

The results of BET analysis show that the addition of GO to ZnO has no influence on SSA while having a slight influence on the total pore volume, which increase from 0.298 cm^3/g for ZnO via 0.348 cm^3/g for ZnO/0.1GO to 0.353 cm^3/g for ZnO/0.5GO, Table 1.

3.2. Photoelectrocatalytic Activity of ZnO/r*x*GO Particles

ZnO/r*x*GO modified GCEs were tested as both anode and cathode depending on the applied potential interval. The overall water splitting reaction mechanism depends on the nature of the electrolyte—whether it is acidic or alkaline—and may be expressed by two half-reactions [69]:

In acidic electrolytes:
(HER on) cathode: $4H^+ + 4e^- \longrightarrow 2H_2$
(OER on) anode: $2H_2O \longrightarrow O_2 + 4H^+ + 4e^-$
Total: $2H_2O \longrightarrow 2O_2 + 2H_2$

In alkaline electrolytes:
(HER on) cathode: $4H_2O + 4e^- \longrightarrow 2H_2 + 4OH^-$
(OER on) anode: $4OH^- \longrightarrow O_2 + 2H_2O + 4e^-$
Total: $2H_2O \longrightarrow 2O_2 + 2H_2$

The catalytic activity of the microwave-processed ZnO/r*x*GO particles toward HER and OER in 0.1 M NaOH and 0.1 M H_2SO_4 was examined in the dark, i.e., as electrocatalysts, and under illumination, i.e., as photoelectrocatalysts, using linear sweep voltammetry (LSV), Figure 3. The representative values for OER activity, the current densities at 2.2 V vs. RHE and the onset potentials (vs. RHE) at 2 mA cm^{-2} are listed in Table 2. We found that in the alkaline medium, the ZnO/r0.5GO composite showed the highest current density of 37.68 mA cm^{-2} under illumination, compared to 26.81 mA cm^{-2} measured in the dark. Simultaneously, the onset potential decreased from 1.636 V to 1.561 V vs. RHE under illumination, indicating enhanced OER kinetics for ZnO/r0.5GO. The ZnO/r0.1GO composite showed somewhat lower activity, reflected in a smaller increase in current density from 11.91 to 19.98 mA cm^{-2} and a shift in onset potential from 1.751 to 1.63 V vs.

RHE. ZnO showed the lowest PEC response, with current density increasing from 7.52 to 9.11 mA cm^{-2} and a minimal reduction in onset potential from 1.847 to 1.828 V vs. RHE.

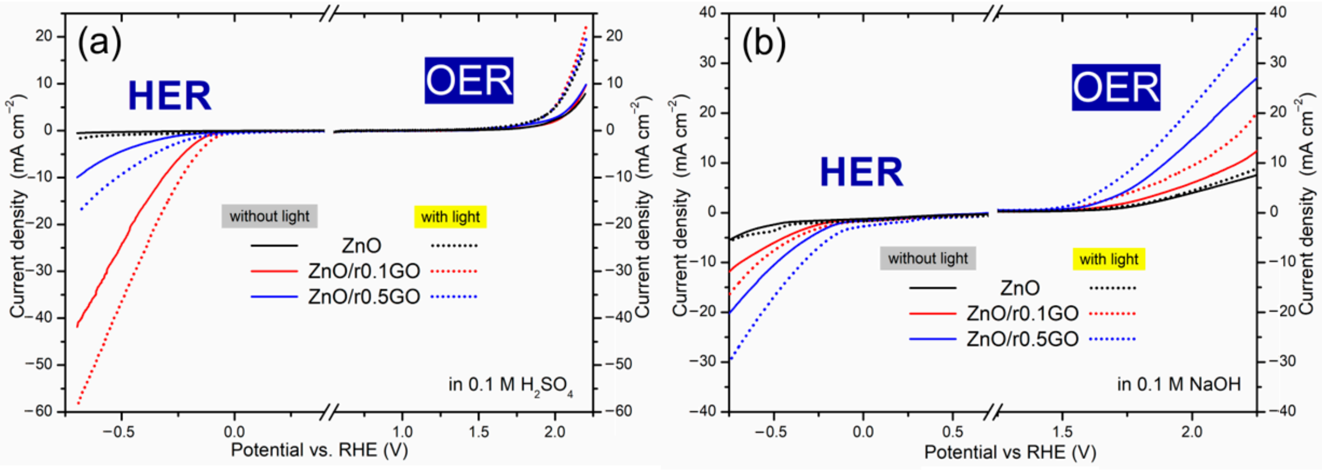

Figure 3. LSVs of ZnO/*rx*GO materials in: (**a**) 0.1 M H_2SO_4, and (**b**) 0.1 M NaOH electrolyte recorded before and after 60 min under illumination.

In the acidic medium, all samples exhibited significantly lower OER activity compared to the alkaline solution. Specifically, higher onset potentials were observed both in the dark and under illumination, while the current densities were consistently lower. The ZnO/r0.1GO composite achieved the highest current density under illumination (21.23 mA cm^{-2}), compared to 9.36 mA cm^{-2} in the dark. The onset potential decreased to 1.724 V vs. RHE under illumination, corresponding to a cathodic shift of 158 mV relative to the dark. The ZnO/r0.5GO composite showed a similar trend, with the current density approximately redoubling from 9.36 to 18.75 mA cm^{-2} under illumination, accompanied by a similar shift in onset potential. In contrast, ZnO showed the most significant reduction in onset potential of 190 mV, while the current density had the lowest value of all samples, both in the dark and under illumination.

The LSVs of ZnO/*rx*GO materials and the representative values for HER activity, the current densities at −0.8 V vs. RHE and the onset potentials (vs. RHE) at 2 mA cm^{-2} in acidic (H_2SO_4) and 3 mA cm^{-2} in alkaline media (NaOH), in dark conditions and under illumination, are presented in Figure 3 and Table 2.

In the acidic medium, the ZnO/r0.1GO composite shows excellent catalytic activity for HER, exhibiting the highest current density and the lowest onset potential. Precisely, the current density was 58.59 mA cm^{-2} V vs. RHE under illumination, compared to 41.13 mA cm^{-2} in the dark at the same potential. The onset potential shifted from −0.113 to −0.066 V vs. RHE, indicating improved reaction kinetics under illumination. The ZnO/r0.5GO composite showed an increase in current density from 9.96 to 17.31 mA g^{-1} with an onset potential shift from −0.247 to −0.113 V vs. RHE. Pure ZnO showed low current density and adverse onset potentials of −0.702 V in the dark and −0.595 V after illumination vs. RHE in acidic medium, indicating poor HER activity.

In the alkaline medium, the ZnO/r0.5GO composite achieved the highest current density of 27.17 mA cm^{-2} under illumination compared to 18.18 mA cm^{-2} in the dark, accompanied by a remarkable onset potential shift from −0.201 to −0.067 V vs. RHE. The ZnO/r0.1GO composite showed an increase in current density from 10.27 to 14.28 mA cm^{-2} with an onset potential shift from −0.307 to −0.241 V vs. RHE. Pure ZnO showed no photoresponse under alkaline HER conditions, maintaining the same current density of 4.32 mA cm^{-2} with a negligible onset potential change from −0.580 to −0.458 V vs. RHE.

In acidic medium, the HER proceeds via direct H^+ reduction and primarily depends on active sites and the efficiency of electron transport. A larger particle surface of ZnO/r0.1GO, due to the platelike morphology and more developed (0001) plane, provides a larger number of active sites, which directly influences its enhanced HER performance compared to ZnO and ZnO/r0.5GO. The OER mechanism in acidic medium is a multi-step process and is more complex. Surface defects promote an earlier onset of the reaction, as observed for ZnO/r0.5GO, whereas a larger particle surface results in higher current densities once the reaction is started, as in the case of ZnO/r0.1GO.

In alkaline medium, water dissociation is the main step in both HER and OER. The presence of surface defects enhances the adsorption and activation of water molecules. Therefore, the ZnO/r0.5GO composite, characterized by the highest defect density, exhibits superior catalytic activity for both reactions in an alkaline electrolyte.

Moreover, the presence of even a small concentration of rGO in the composite significantly improves charge transfer for HER and OER in both electrolytes [70]. By providing a highly conductive network, rGO enables faster electron transport, reduces Ohmic losses, and thus enhances the overall catalytic performance of the composite materials.

Previously, it has been shown that the photoelectrocatalytic activity of ZnO for overall water splitting extensively depends on the crystallinity, crystallite size and polarity, along with the particle size [10,71–73]. In particular, for metal oxide-based photocatalysts, it has been verified that hexagonal platelike crystals exhibit 5-fold better photocatalytic activity than rodlike ones, where the improved activity of platelike crystals has been explained by ZnO's crystalline structure [71–73]. Actually, ZnO has a Wurtzite crystalline structure with layers containing either all positive Zn^{2+} ions or all negative O_2 ions stacked alternatively along the [0001] direction, resulting in the Zn-terminated (0001) and O-terminated (000-1) polar planes [73]. The terminal polar planes (0001) and (000-1) were reported to be much more active in photocatalysis as compared to the nonpolar facets perpendicular to them (for example 1-100, or 01-10), mainly due to a higher density of defects such as oxygen vacancies. The addition of graphene oxide significantly affects the crystallite polarity and morphology of ZnO particles prepared by the microwave processing of the precipitate.

Table 2. Current density and onset potential of ZnO/rxGO materials for HER and OER in alkaline and acidic electrolytes recorded before and after 60 min under illumination, along with literature-reported data.

Materials	Current Density (mAcm^{-2})		Onset Potential vs. RHE (V)		Reference
	Dark	Illumination	Dark	Illumination	
OER in 0.1 M NaOH					
ZnO	7.52	9.11	1.847	1.828	This paper
ZnO/r0.1GO	11.91	19.98	1.751	1.630	
ZnO/r0.5GO	26.81	37.68	1.636	1.561	
$2ZnO/1RuO_2$	N/A	N/A	1.737	1.566	[13]
$10ZnO@RuO_2$	N/A	N/A	2.06	1.96	[12]
OER in 0.1 M KOH					
RGO-ZnO	N/A	N/A	1.614	N/A	[74]
ZnO@rGO	N/A	N/A	1.700	N/A	[75]
CuO/ZnO@rGO	N/A	N/A	1.678	N/A	[5]
OER in 0.5 M KOH					
$RGO/CuWO_4/Ti_3C_2T_x$	7.0	8.5	0.5	0.6	[76]

Table 2. *Cont.*

Materials	Current Density (mAcm^{-2})		Onset Potential vs. RHE (V)		Reference
	Dark	Illumination	Dark	Illumination	
OER in 0.1 M H_2SO_4					
ZnO	7.67	17.34	1.882	1.692	This paper
ZnO/r0.1GO	9.36	21.23	1.882	1.724	
ZnO/r0.5GO	9.36	18.75	1.752	1.724	
10ZnO@RuO_2	2.15	2.01	N/A	N/A	[12]
HER in 0.1 M NaOH					
ZnO	4.32	4.32	−0.580	−0.458	This paper
ZnO/r0.1GO	10.27	14.28	−0.307	−0.241	
ZnO/r0.5GO	18.18	27.17	−0.201	−0.067	
2ZnO/1RuO_2	N/A	N/A	−0.238	−0.164	[13]
10ZnO@RuO_2	N/A	N/A	−0.348	−0.376	[12]
HER in 1 M KOH					
CuO/ZnO@rGO	N/A	N/A	−0.358	N/A	[5]
HER in 0.5 M KOH					
ZnO/rGO	N/A	N/A	−0.755	N/A	[77]
RGO/$CuWO_4$/$Ti_3C_2T_x$	1.7	2.0	−0.100	−0.100	[76]
ZG0.5	10	15	−0.659	−0.600	[77]
HER in 0.1 M H_2SO_4					
ZnO	0.34	1.68	−0.702	−0.595	This paper
ZnO/r0.1GO	41.13	58.59	−0.113	−0.066	
ZnO/r0.5GO	9.96	17.31	−0.247	−0.113	
10ZnO@RuO_2	N/A	N/A	−0.714	−0.526	[12]
WS_2/ZnO	N/A	N/A	−0.201	−0.182	[78]
HER in 0.5 H_2SO_4					
rGO	N/A	N/A	−0.1	N/A	[79]
Au/rGO	N/A	N/A	−0.05	N/A	
PtAu/rGO	N/A	N/A	−0.005	N/A	
RGO-ZnO	N/A	N/A	−0.348	N/A	[74]

For additional insight into the catalytic activity of the ZnO/r*x*GO materials, the overpotential at 10 mA cm^{-2} (η_{10}) and the turnover frequency (TOF) were determined for HER and OER in both electrolytes under dark and illuminated conditions; the calculated η_{10} and TOF values are displayed in Table 3. The calculated η_{10} and TOF values are consistent with the trends observed for the onset potential and current density, i.e., ZnO/r0.5GO demonstrates the lowest overpotential and highest TOF for both HER and OER in alkaline medium, while ZnO/r0.1GO shows superior activity for HER in acidic medium.

Table 3. TOF and η_{10} of ZnO/rxGO materials for HER and OER in alkaline and acidic electrolytes recorded before and after 60 min under illumination.

	TOF (s^{-1})		**η_{10} (V vs. RHE)**	
	Dark	**Illumination**	**Dark**	**Illumination**
		OER in 0.1 M NaOH		
ZnO	6.02	10.24	N/A	N/A
ZnO/r0.1GO	17.14	32.22	0.961	0.790
ZnO/r0.5GO	28.82	51.74	0.661	0.572
		OER in 0.1 M H_2SO_4		
ZnO	1.68	8.46	N/A	0.862
ZnO/r0.1GO	1.98	9.98	N/A	0.862
ZnO/r0.5GO	1.65	8.29	0.972	0.851
		HER in 0.1 M NaOH		
ZnO	20.91	29.33	N/A	N/A
ZnO/r0.1GO	40.45	49.71	−0.685	−0.585
ZnO/r0.5GO	53.81	95.52	−0.478	−0.333
		HER in 0.1 M H_2SO_4		
ZnO	0.14	9.13	N/A	N/A
ZnO/r0.1GO	106.62	186.85	−0.315	−0.230
ZnO/r0.5GO	13.38	35.45	−0.690	−0.510

For OER in both alkaline and acidic media, ZnO/r0.5GO showed the lowest overpotential among the investigated samples, with η_{10} values of 0.661 V and 0.572 V in the dark and under illumination in alkaline medium, and 0.972 and 0.851 V in the dark and under illumination in acidic medium, respectively. Bare ZnO did not reach the current density of 10 mA cm^{-2} within the investigated potential window in either medium in the dark and under illumination in alkaline medium, while ZnO/rGO_0.1 did not reach this value in acidic medium in the dark, indicating poor OER activity under these conditions. ZnO and ZnO/r0.1GO showed η_{10} values of 0.862 V under illumination in acidic medium, similar to ZnO/r0.5GO. The TOF values increased in the order ZnO < ZnO/r0.1GO < ZnO/r0.5GO under both conditions in alkaline medium, with ZnO/r0.5GO achieving the highest values of 28.82 and 51.74 s^{-1} in the dark and under illumination, respectively. The TOF values were significantly lower for all samples in acidic medium compared to alkaline, consistent with the overpotential, onset potential, and current density values obtained for OER under these conditions.

For HER in alkaline medium, ZnO/r0.5GO exhibited the lowest overpotential and the highest TOF among the investigated samples, with η_{10} values of −0.478 and −0.333 V, and TOF of 53.81 and 95.52 s^{-1} in the dark and under illumination, respectively. ZnO/r0.1GO showed η_{10} of −0.685 and −0.585 V, and TOF of 40.45 and 49.71 s^{-1} in the dark and under illumination, respectively, while pure ZnO did not achieve 10 mA cm^{-2} in alkaline medium. In acidic medium, ZnO/r0.1GO showed the lowest overpotential with η_{10} of −0.315 and −0.230 V, and the highest TOF of 106.62 and 186.85 s^{-1} in the dark and under illumination, respectively, significantly exceeding those of ZnO/r0.5GO (13.38 and 35.45 s^{-1}) and bare ZnO (0.14 and 9.13 s^{-1}). The same trend was observed upon comparison of the onset potential and current density values.

3.3. Electroanalytical Measurements of Microwave-Processed ZnO/rxGO Particles

3.3.1. Determination of EASA and k^0

Figure 4a shows CVs of GCEs modified with ZnO/*rx*GO materials, recorded in 5 mM $K_4[Fe(CN)_6]$ with 0.1 M KCl as the supporting electrolyte. Based on these measurements, two important electrochemical parameters—EASA (Figure 4b) and k^0 (Figure 4c)—were estimated for all three investigated materials. EASA values decrease in the following order: ZnO/r0.5GO (1.315 cm^2) > ZnO (1.289 cm^2) > ZnO/r0.1GO (1.092 cm^2). The k^0 values indicate that the addition of GO to ZnO increases the heterogenous electron transfer rate constant of ZnO/r0.5GO ($0.826 \cdot 10^{-3}$ cm s^{-1}) and ZnO/r0.1GO ($1.173 \cdot 10^{-3}$ cm s^{-1}) for 28 and 82%, respectively, compared to ZnO ($0.644 \cdot 10^{-3}$ cm s^{-1}). Overall, the improved k^0 values suggest enhanced charge transfer kinetics for the ZnO/rxGO composites compared to pure ZnO.

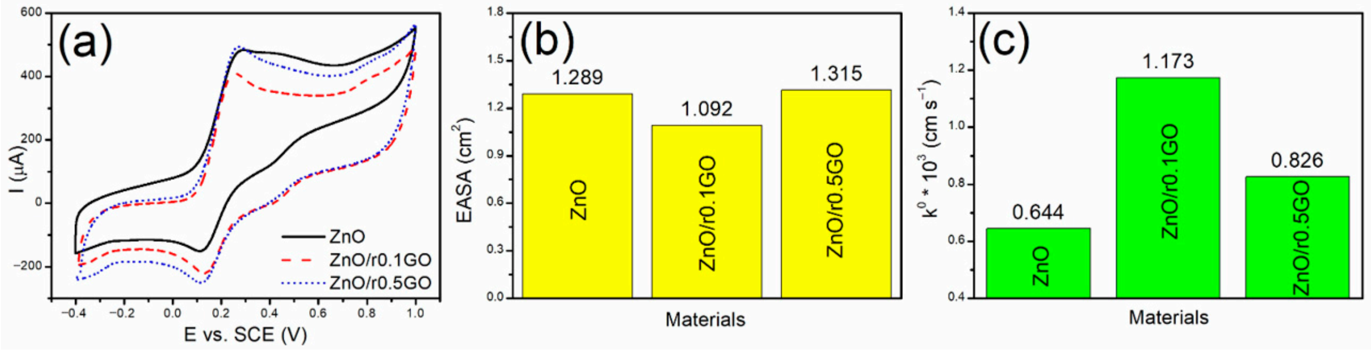

Figure 4. (**a**) Cyclic voltammograms of ZnO/*rx*GO materials, recorded in 5 mM $K_4[Fe(CN)_6]$ with 0.1 M KCl as supporting electrolyte, at a scan rate of 20 mV s^{-1}, with the corresponding (**b**) EASA, and (**c**) k^0 values.

3.3.2. Electroanalytical Measurements

Figure 5 presents the electrochemical response of the investigated materials for different diclofenac concentrations. As shown in Figure 5a–c, two well-defined characteristic anodic peaks were observed. The anodic peak located at around 550 mV vs. SCE is assigned to the direct electrochemical oxidation of diclofenac, and the products obtained are 2,6-dichloroaniline and 2-(2-hydroxyphenyl) acetic acid. The second anodic peak, appearing at approximately 300 mV vs. SCE, is attributed to the oxidation of 1-hydroxy-2-(hydroxyphenyl)ethanolate, a product of the electrochemical transformation of diclofenac [80]. This oxidation process of diclofenac is shown in Scheme 1. In accordance with the literature reports, diclofenac can therefore be determined both directly and indirectly through the anodic peaks at 550 mV and 300 mV, respectively [81].

Based on the anodic peak current responses obtained by LSV, calibration curves were constructed for both direct and indirect determination of diclofenac. The corresponding calibration plots for each investigated material are presented in Figure 5d–f, while the calculated relevant statistical and electroanalytical parameters are summarized in Figure 6 and Table 4. ZnO displays two linear fitting ranges for diclofenac detection, whereas ZnO/rGO composites exhibit a single linear region described by one calibration line, for both direct and indirect approaches. ZnO exhibited the closest agreement with the linear fit showing the correlation coefficient (R^2) of 0.998 for the second calibration line at 550 mV. The lowest R^2 value observed is 0.944 (ZnO/r0.1GO at 550 mV), indicating strong agreement for all measurements.

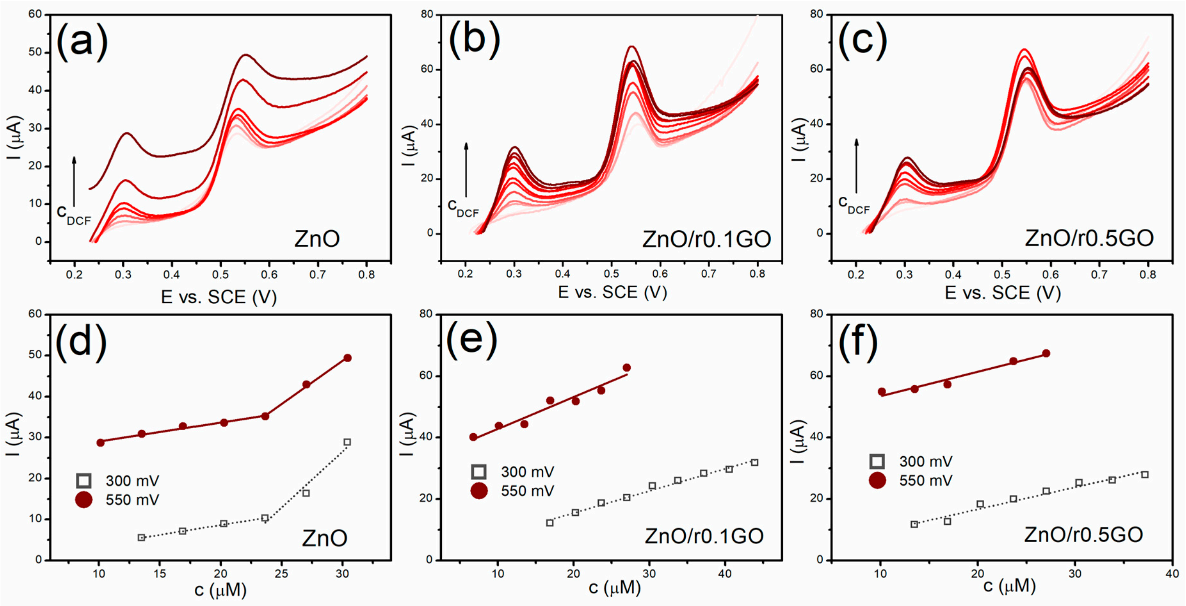

Figure 5. (**a**–**c**) LSVs of ZnO/r*x*GO materials recorded in the neutral 0.1 M phosphate buffer, with the addition of diclofenac and at scan rate of 20 mV s^{-1}, and (**d**–**f**) the corresponding calibration plots.

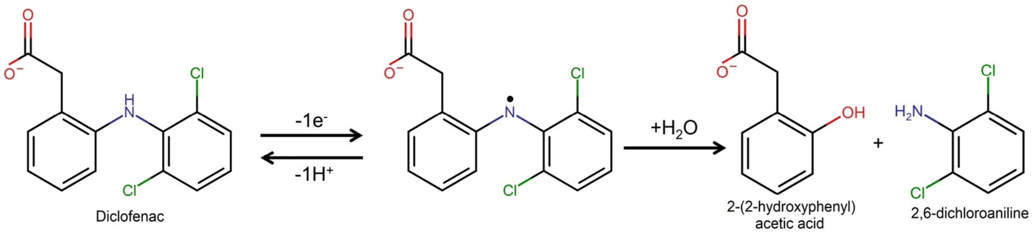

Scheme 1. Electrochemical oxidation of diclofenac (the freeware ChemSketch computing program was used to draw the molecules).

As presented in Table 4, pure ZnO showed the highest sensitivities for diclofenac detection, reaching 2.728 $\mu A \mu M^{-1}$ (300 mV) and 2.108 $\mu A \mu M^{-1}$ (550 mV); however, these enhanced sensitivities are achieved only within very narrow concentration intervals defined by the second linear regions. In contrast, ZnO/rGO composites display moderate but uniform sensitivities described by a single calibration line, with ZnO/r0.1GO showing the highest sensitivity among the composites (1.040 $\mu A \mu M^{-1}$ at 550 mV) (Figure 6a). Lochab et al. investigated an indium tin oxide electrode with asparagine-functionalized multi-walled carbon nanotubes and ionic liquid (Asp-MWCNTs/IL/ITO) for electrochemical detection of diclofenac in neutral media by the CV method [82]. All tested ZnO/r*x*GO materials showed comparable or higher sensitivity values than those reported for Asp-MWCNTs/IL/ITO (0.4657 $\mu A \mu M^{-1}$) and significantly higher than was found for glassy carbon electrodes modified with copper nanoparticles and reduced graphene oxide (Cu NPs/rGO/GCE) by the amperometry method in 0.1 M Na_2SO_4 (pH = 7.0) proposed by Yu et al. (0.0356 $\mu A \mu M^{-1}$) [83] (Table 4). The lowest LOD/LOQ values (Figure 6b,c) were obtained for ZnO, 2.2/7.3 μM at 300 mV and 4.4/14.8 μM (at 550 mV), followed by ZnO/r0.1GO which showed values of 4.4/14.7 μM with detection at 300 mV. ZnO/rGO composites exhibit slightly higher but comparable detection and quantification limits. Additionally, it should be noted that for the same material, lower LOD/LOQ values are obtained for indirect determination at 300 mV. Comparison with the literature data (Table 4) reveals that previously reported studies typically exhibit comparable or lower detection limits than those obtained in this study. In contrast to pure ZnO, which shows narrow and separated dynamic ranges, ZnO/rGO composites offer a single, broader dynamic range, making them more suitable for practical sensing applications. The widest dynamic range of 16.9–43.9 µM is obtained for the ZnO/r0.1GO composite at 300 mV (Figure 6d). Aidli et al. proposed an electrochemical sensor that features a benzoquinone-modified vertically aligned mesoporous silica film on a carbon screen-printed electrode (BQ/VMSF/aSPCE) for diclofenac detection in neutral phosphate buffer by the DPV method [84]. BQ/VMSF/aSPCE, as well as the aforementioned Asp-MWCNTs/IL/ITO, exhibited narrower linearity ranges (1–10 µM and 0.0675–0.54 µM, respectively) than presented herein, while oxygen plasma-treated ZnO nanoflowers on a screen-printed electrode proposed in the work of Zhang et al. [29] showed a linearity region as wide as 0.01–40 µM (Table 4). These findings indicate that the ZnO/r0.1GO composite demonstrates the most balanced electroanalytical performance for diclofenac detection, offering an extended dynamic range while still preserving sufficiently low LOD at 300 mV. The superior sensing behavior of ZnO/r0.1GO compared to ZnO and ZnO/r0.5GO correlates with its highest k^0 value and relatively high EASA, indicating that the synergistic interaction between ZnO and rGO facilitates more efficient electron transfer, as well as promoting an active surface of the electrochemical sensor.

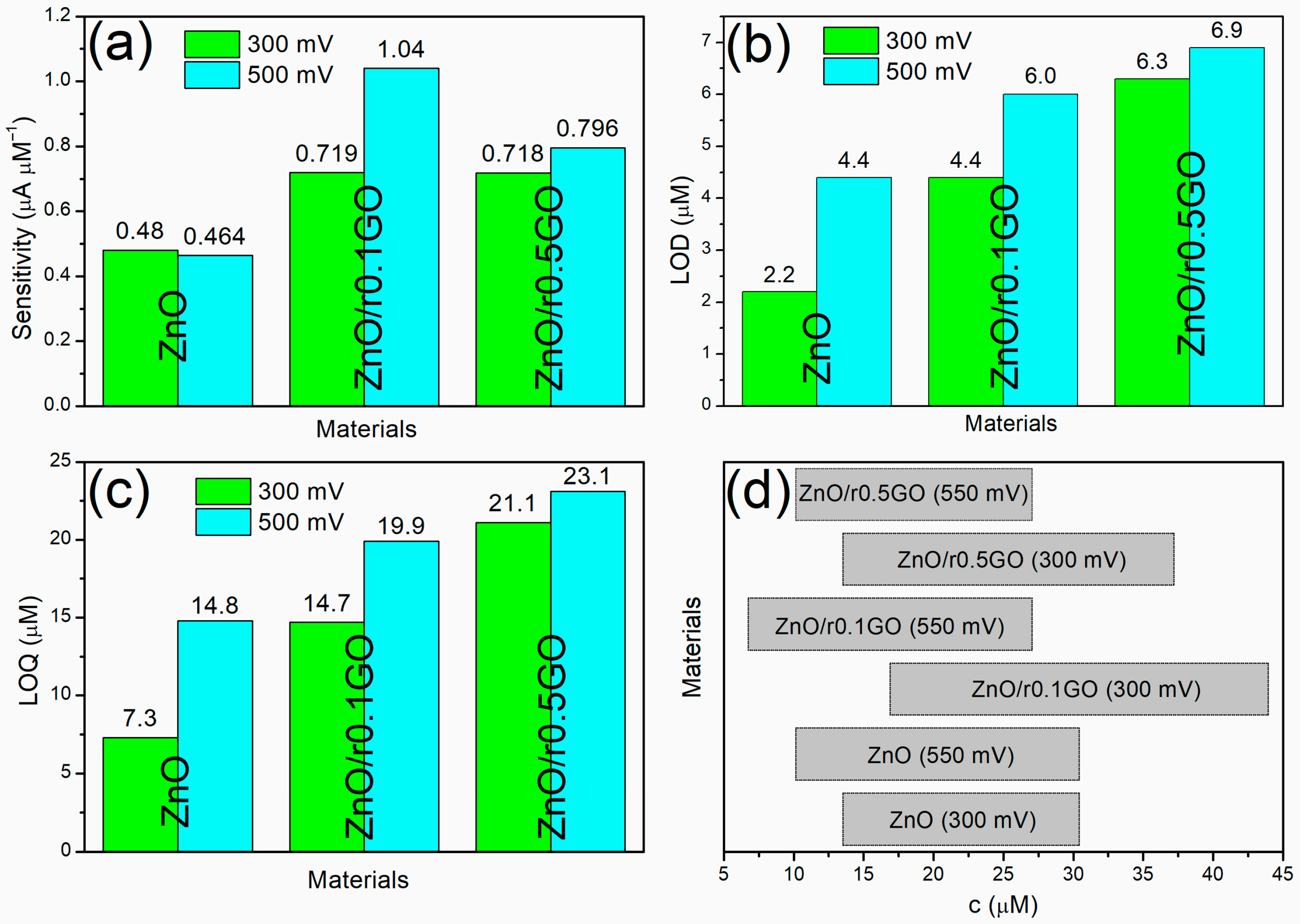

Figure 6. (**a**) Sensitivity, (**b**) limits of detection, (**c**) limits of quantification, and (**d**) dynamic ranges of ZnO/r*x*GO materials for direct and indirect determination of diclofenac in neutral phosphate buffer.

Table 4. Statistical and electroanalytical parameters for diclofenac detection obtained for ZnO/*rx*GO, along with literature-reported materials.

Electrode	**Method**	**Peak Potential (mV)**	**R^2**	**Sensitivity (μAμM^{-1})**	**LOD (μM)**	**LOQ (μM)**	**Dynamic Range (μM)**	**References**
Electrolyte 0.1 M phosphate buffer (pH = 7.0)								
ZnO	LSV	300 (first line)	0.997	0.480	2.2 (0.6 ppm)	7.3 (2.2 ppm)	13.5–30.4	This paper
		300 (second line)	0.961	2.728	/	/		
		550 (first line)	0.979	0.464	4.4 (1.3 ppm)	14.8 (4.4 ppm)	10.1–30.4	
		550 (second line)	0.998	2.108	/	/		
ZnO/r0.1GO	LSV	300	0.985	0.719	4.4 (1.3 ppm)	14.7 (4.4 ppm)	16.9–43.9	This paper
		550	0.944	1.040	6.0 (1.8 ppm)	19.9 (5.9 ppm)	6.8–27.0	
ZnO/r0.5GO	LSV	300	0.963	0.718	6.3 (1.9 ppm)	21.1 (6.2 ppm)	13.5–37.2	This paper
		550	0.959	0.796	6.9 (2.0 ppm)	23.1 (6.8 ppm)	10.1–27.0	
BQ/VMSF/aSPCE	DPV	/	0.996	/	0.73	/	1–10	[84]
Asp-MWCNTs/IL/ITO	CV	/	0.9885	0.4657	0.0094	/	0.0675–0.54	[82]
Gd_2O_3/Graphene	DPV	/	/	/	0.028	0.086	5.89–66.7	[85]
Electrolyte 0.1 M Na_2SO_4 (pH = 7.0)								
Cu NPs/rGO/GCE	A*	/	/	0.0356	0.008	/	20–400	[83]

A*—amperometry.

3.4. DFT Calculations

Initially, the diclofenac molecule was bonded on the (000-1) ZnO surface via a hydrogen atom from the 2,6-dichlorophenyl ring, but after the relaxation, the molecule was slightly shifted and relaxed in the vicinity of the surface. This resulted in interatomic H-O distances between hydrogen ions from the molecule and oxygen ions from the surface of 2.18 and 2.21 Å, respectively. Bond orders and charge overlap analyses by the DDEC6 method [56] shows that these bonds have orders of 0.382 and 0.336 while mutual overlaps cover 0.335 and 0.312 e^-. According to the Bader analysis, zinc ions in the highest Zn-layer of the (000-1) ZnO surface mainly lose an average of 0.02 to 0.06 e^- while oxygen ions from the highest O-layer received more electrons on average, mostly from 0.07 to 0.15 e^- in interaction with the molecule relative to the e^- transfer on the pure (000-1) ZnO's surface, Figure 7a.

After the relaxation of the system consisted of a diclofenac molecule and reduced graphene, the distances between the hydrogen ions (H) in the phenyl ring of the diclofenac molecule and the nearest carbon (C) atoms in the graphene slab are 2.76, 2.87, and 2.97 Å. These increased distances are partly due to a descent of the carbon atoms under the molecule from the initial plane up to 0.55 Å as a consequence of the interaction between the diclofenac molecule and the graphene. The DDEC6 analysis shows that the mentioned C-H bonds have bond orders of 0.023, 0.047, and 0.045 overlapping up to 0.038 e^-. The results obtained by the DDEC6 calculation suggest that the possibility of the diclofenac molecule chemically bonding to the graphene slab is negligible.

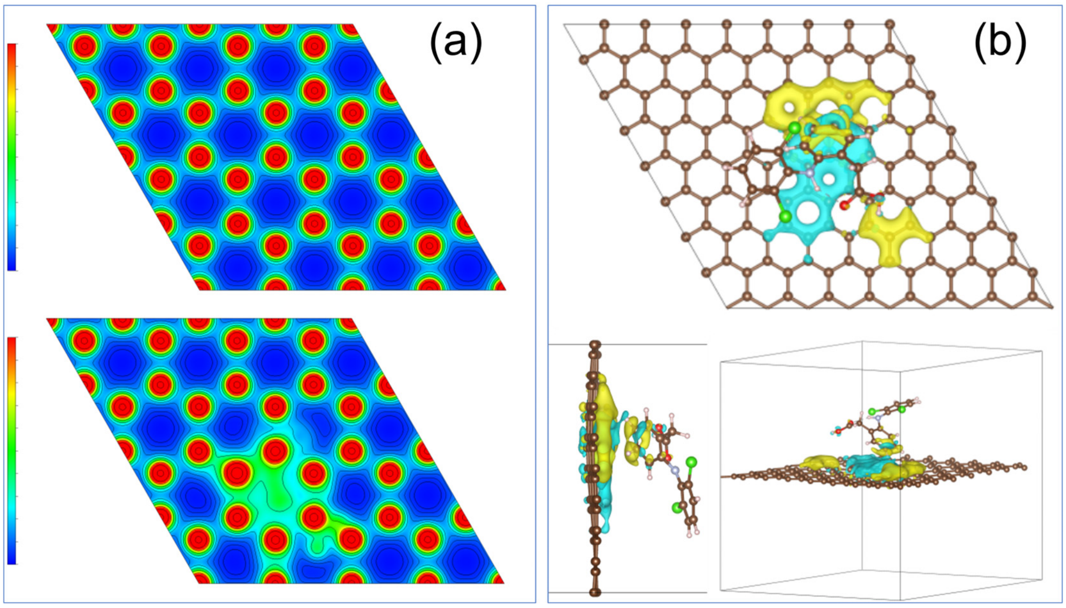

Figure 7. (**a**) The view of charge density of ZnO (000-1) surface along (00-1) direction without (**top**) and with (**bottom**) diclofenac molecule (DCF) in its vicinity. Colors depict e$^-$ density from the lowest (blue) to the highest (red) [86]. (**b**) The charge difference of the diclofenac–graphene system $\Delta\varrho = \varrho_{ZnO+DCF} - \varrho_{ZnO} - \varrho_{DCF}$ is obtained by applying the VASPKIT software (Version 1.5.1) [87] on self-consistently converged charge densities, where $\varrho_{ZnO+DCF}$, ϱ_{ZnO}, and ϱ_{DCF}, are the charge densities of the complex consisting of the ZnO surface and diclofenac molecule on top of it, ideal ZnO surface, and the diclofenac molecule, respectively. The electron redistribution is depicted by VESTA software (Version 3.90.0a) [86]; yellow (electron-enriched area) represents the positive and cyan represents the negative charge difference. The view from the top of the c-axis (**top**), from the top of the b-axis (**bottom left**) and a general view (**bottom right**).

The carbon atoms under the molecule lose up to 0.09 e$^-$. The electric dipole moment of the molecule calculated relative to the molecule mass center has a direction almost parallel with the x–y plane (theta = 89.93 degrees), and an azimuth angle phi = −54.75 degrees. This direction matches the negative–positive charge areas of graphene (see Figure 7b). Such a position of the molecule relative to the surface may indicate the existence of long-range electromagnetic interactions that hold the molecule near the graphene slab.

In this case the calculated adsorption binding energy of the diclofenac–graphene complex is +0.092 eV whereas for the diclofenac-(000-1) ZnO it is −3.60 eV. Results of the DFT calculations show that diclofenac exhibits a weak chemical interaction/chemisorption with the (000-1) ZnO surface, while it does not bond to the graphene layer. This result suggests that in the composite, ZnO contributes to the binding with the pollutant molecule, while the reduced graphene oxide predominantly affects the charge redistribution and electron mobility.

Results of the ab initio calculations support experimental results which we presented in this paper and our conclusion that the improved electrochemical activity of ZnO/*x*GO compared with bare ZnO is due to platelike particles consisting of well-developed crystallites with a displayed (000-1) surface.

4. Conclusions

We established that a relatively small amount of GO used as seeds for precipitation of $Zn(OH)_2$ influenced crystallite growth and polarity in spite of the short period of microwave irradiation. The presented results show that the addition of GO to ZnO influences the crystal structure ordering, particle morphology, the amount of surface and bulk defects and visible light absorption capacity. The synergy of these properties significantly enhanced the electrochemical properties of ZnO/r*x*GO particles.

We reveal that in alkaline medium, the ZnO/r0.5GO composite exhibits the highest catalytic activity for HER and OER in the dark as well as under illumination. Precisely, with ZnO/r0.5GO as the photoelectrocatalyst under illumination, the current density attained was 37.68 mA cm^{-2} and the onset potential was 1.561 V vs. RHE for OER, and the current density was 27.17 mA cm^{-2} and the onset potential was -0.067 V vs. RHE for HER. In acidic medium, all samples exhibited similar activity for OER but ZnO/r0.1GO composite demonstrated the highest activity for HER in the dark and under illumination; i.e., under illumination the current density attained was 58.59 mA cm^{-2} V vs. RHE and the onset potential was -0.066 V vs. RHE.

Due to having the fastest charge transfer rate ($k^0 = 1.173 \times 10^{-3}$ cm s^{-1}) and favorable electrochemically active surface area, the composite exhibited the best analytical performance as the electrochemical sensor for diclofenac in a neutral environment. ZnO/r0.1GO showed the broadest dynamic range of 16.9–43.9 μM at 300 mV and a sufficiently low LOD of 4.4 μM.

This study demonstrates that the addition of small amounts of GO to ZnO represents an effective strategy for tailoring the surface properties and charge transfer characteristics of the ZnO/*x*GO composites, enabling their application as a multifunctional material for photoelectrocatalytic water splitting and electrochemical detection of diclofenac as a water pollutant. The results highlight the importance of rGO content as a key parameter in controlling the balance between surface area and defect density, which is significant for specific applications such as water splitting or the detection of pollutants.

Author Contributions: A.N.: investigation, methodology, and writing—reviewing and editing; M.K.: investigation; K.A.: investigation, methodology, and writing—reviewing and editing; A.S.: investigation; L.V.: investigation; S.Š.: investigation and writing—reviewing and editing; M.K.R.: investigation; V.N.I.: investigation and writing—original draft; J.B.-Č.: investigation and writing—original draft; A.U.: investigation; I.S.S.: conceptualization, methodology, investigation, writing—reviewing and editing, and supervision; S.M.: conceptualization, methodology, investigation, writing—reviewing and editing, and supervision. All authors have read and agreed to the published version of the manuscript.

Funding: This research was supported by the Science Fund of the Republic of Serbia (The Program PRISMA, #7377, Water pollutants detection by ZnO-modified electrochemical sensors: From computational modeling via electrochemical testing to real system application—WaPoDe) and by the Ministry of Science, Technological Development and Innovation of the Republic of Serbia (Contract Nos. 451-03-33/2026-03/200175, 451-03-34/2026-03/200146, and 451-03-33/2026-03/200017).

Data Availability Statement: The data presented in this study are available on request from the corresponding author. The data supporting the findings of this study will be deposited in the repository of the Institute of Technical Sciences of SASA following publication.

Acknowledgments: This paper is dedicated to our colleague Vasil Koteski who suddenly passed away in November 2025. Koteski was the WaPoDe project team member and his results on DFT calculations are included in this paper.

Conflicts of Interest: The authors declare no conflicts of interest.

References

1. Badoni, A.; Thakur, S.; Vijayan, N.; Swart, H.C.; Bechelany, M.; Chen, Z.; Sun, S.; Cai, Q.; Chen, Y.; Prakash, J. Recent Progress in Understanding the Role of Graphene Oxide, TiO_2 and Graphene Oxide-TiO_2 Nanocomposites as Multidisciplinary Photocatalysts in Energy and Environmental Applications. *Catal. Sci. Technol.* **2025**, *15*, 1702–1770. [CrossRef]

2. Kumar, K.R.; Sri, N.D.; Kale, V.N.; Maiyalagan, T. Surface Reconstruction of Mo-Doped NiFe-LDH Nanosheets Decorated on Nitrogen and Sulfur Dual-Doped Reduced Graphene Oxide as a Bifunctional Electrocatalyst for Overall Water Splitting. *Int. J. Hydrogen Energy* **2025**, *101*, 837–847. [CrossRef]
3. Pasindu, V.; Yapa, P.; Dabare, S.; Munaweera, I. Multifunctional Transition Metal Oxide/Graphene Oxide Nanocomposites for Catalytic Dye Degradation, Renewable Energy, and Energy Storage Applications. *RSC Adv.* **2025**, *15*, 33162–33186. [CrossRef]
4. Nastasić, A.; Radinović, K.; Rakočević, L.; Stojadinović, S.; Stanković, D.; Šljukić, B.; Milikić, J. Efficient Cobalt-Based Bimetallic Nanocatalysts with Iron, Manganese, Molybdenum, and Nickel on Reduced Graphene Oxide for Oxygen Evolution Reaction. *J. Power Sources* **2026**, *666*, 239116. [CrossRef]
5. Younas, U.; Mobeen, F.; Saleem, A.; Ali, F.; Al Huwayz, M.; Ashraf, A.; Ahmad, A.; Alwadai, N.; Pervaiz, M.; Iqbal, M. Efficient Hydrogen Production via Overall Water Splitting Using CuO/ZnO Decorated Reduced Graphene Oxide as Bifunctional Electrocatalyst. *Ceram. Int.* **2024**, *50*, 30570–30578. [CrossRef]
6. Al Mahmud, A.; Thalji, M.R.; Dhakal, G.; Haldorai, Y.; Kim, W.K.; Shim, J.J. Bifunctional MoC/NiC@N-Doped Reduced Graphene Oxide Nano Electrocatalyst for Simultaneous Production of Hydrogen and Oxygen through Efficient Overall Electrochemical Water Splitting. *Mater. Today Nano* **2024**, *27*, 100489. [CrossRef]
7. Marlinda, A.R.; Yusoff, N.; Sagadevan, S.; Johan, M.R. Recent Developments in Reduced Graphene Oxide Nanocomposites for Photoelectrochemical Water-Splitting Applications. *Int. J. Hydrogen Energy* **2020**, *45*, 11976–11994. [CrossRef]
8. Yeh, T.F.; Cihlář, J.; Chang, C.Y.; Cheng, C.; Teng, H. Roles of Graphene Oxide in Photocatalytic Water Splitting. *Mater. Today* **2013**, *16*, 78–84. [CrossRef]
9. Saleem, Z.; Pervaiz, E.; Yousaf, M.U.; Niazi, M.B.K. Two-Dimensional Materials and Composites as Potential Water Splitting Photocatalysts: A Review. *Catalysts* **2020**, *10*, 464. [CrossRef]
10. Marković, S.; Stojković Simatović, I.; Ahmetović, S.; Veselinović, L.; Stojadinović, S.; Rac, V.; Škapin, S.D.; Bajuk Bogdanović, D.; Janković Častvan, I.; Uskoković, D. Surfactant-Assisted Microwave Processing of ZnO Particles: A Simple Way for Designing the Surface-to-Bulk Defect Ratio and Improving Photo(Electro)Catalytic Properties. *RSC Adv.* **2019**, *9*, 17165–17178. [CrossRef]
11. Rajić, V.; Stojković Simatović, I.; Veselinović, L.; Čavor, J.B.; Novaković, M.; Popović, M.; Škapin, S.D.; Mojović, M.; Stojadinović, S.; Rac, V.; et al. Bifunctional Catalytic Activity of $Zn_{1-x}Fe_xO$ toward the OER/ORR: Seeking an Optimal Stoichiometry. *Phys. Chem. Chem. Phys.* **2020**, *22*, 22078–22095. [CrossRef]
12. Aleksić, K.; Stojković Simatović, I.; Stanković, A.; Veselinović, L.; Stojadinović, S.; Rac, V.; Radmilović, N.; Rajić, V.; Škapin, S.D.; Mančić, L.; et al. Enhancement of $ZnO@RuO_2$ Bifunctional Photo-Electro Catalytic Activity toward Water Splitting. *Front. Chem.* **2023**, *11*, 1173910. [CrossRef]
13. Aleksić, K.; Stojković Simatović, I.; Popović, M.; Belošević-Čavor, J.N.; Mančić, L.; Marković, S. Photoelectrocatalytic Activity of ZnO/RuO_2 Composites Toward HER and OER Reactions: The Importance of Surface and Bulk Oxygen Vacancies. *Processes* **2025**, *13*, 2943. [CrossRef]
14. Bounegru, A.V.; Dinu Iacob, A.; Iticescu, C.; Georgescu, P.L. Electrochemical Sensors and Biosensors for the Detection of Pharmaceutical Contaminants in Natural Waters—A Comprehensive Review. *Chemosensors* **2025**, *13*, 65. [CrossRef]
15. Guo, H.; Fan, X.; Chen, J.; Lv, M.; Li, L.; Guo, H.; Ma, M. A synergistic interfacial engineering of NH_2-MIL-125(Ti)/$Ti_3C_2T_x$ heterojunction for sensing methyl parathion. *Microchem. J.* **2026**, *221*, 116985. [CrossRef]
16. Li, J.; Li, L.; Fei, J.; Zhao, P.; Zhao, J.; Xie, Y. Ultrasensitive electrochemical sensor for fenitrothion based on MIL-125 derived iron/titanium bimetallic oxides doped porous carbon composite. *Microchem. J.* **2024**, *200*, 110426. [CrossRef]
17. Dube, A.; Malode, S.J.; Alshehri, M.A.; Shetti, N.P. Recent advances in the development of electrochemical sensors for detecting pesticides. *J. Ind. Eng. Chem.* **2025**, *144*, 77–99. [CrossRef]
18. Gavran, A.; Uskoković-Marković, S.; Nedić Vasiljević, B.; Janošević Ležaić, A.; Gavrilov, N.; Milojević-Rakić, M.; Bajuk-Bogdanović, D. Tracking PFAS Using Nanomaterial-Based Sensors: Limitations, Advances, and Challenges. *Chemosensors* **2025**, *13*, 421. [CrossRef]
19. Lee, A.; Orr, R.; Sanchez-Almirola, J.; Casals-Terré, J.; Kaushik, A. Can Smart Electrochemical Sensors Sustainably Tackle PFAS-@Microplastics? *ECS Sens. Plus* **2025**, *4*, 033402. [CrossRef]
20. Khadka, M.; Pasternak, Y.M.; Sheinenzon, O.; Snezhko, A.; Ronen, A.; Amiram, M.; Ben-Yoav, H. Detection of perfluorooctance sulphonic acid in groundwater using an intelligent array of electrochemical sensors. *J. Hazard. Mater.* **2025**, *495*, 138844. [CrossRef]
21. Wu, J.; Yue, X.; Wang, T.; Zhang, Y.; Jin, Y.; Li, G. A cost-effective and sensitive voltammetric sensor for determination of baicalein in herbal medicine based on shuttle-shape α-Fe_2O_3 nanoparticle decorated multi-walled carbon nanotubes. *Colloids Surf. A Physicochem. Eng. Asp.* **2025**, *717*, 136850. [CrossRef]
22. Radinović, K.; Milikić, J.; Gavrilov, N.; Stanković, D.; Basak, A.; Metin, Ö.; Šljukić, B. Facile synthesis of Co/rGO, Au/rGO, and CoAu/rGO Nanocomposites for Precise Determination of Arsenic(III) in Water Systems. *Electrochim. Acta* **2024**, *507*, 145147. [CrossRef]

23. Saisree, S.; Arya, S.; Nair, E.D.; Sandhya, K.Y. Electrochemical sensors for monitoring water quality: Recent advances in graphene quantum dot-based materials for the detection of toxic heavy metal ions Cd(II), Pb(II) and Hg(II) with their mechanistic aspects. *J. Environ. Chem. Eng.* **2025**, *13*, 116545. [CrossRef]
24. Zhang, Z.; Liu, H.; Wang, Z.; Majdi, A.; Wang, G.; Salameh, A.A.; AL-Huqail, A.A.; Elhosiny Ali, H. Electrochemical monitoring sensors of water pollution systems. *Food Chem. Toxicol.* **2022**, *166*, 113196. [CrossRef]
25. Nakhjavani, S.A.; Mirzajani, H.; Carrara, S.; Onbaşlı, M.C. Advances in biosensor technologies for infectious diseases detection. *Trends Anal. Chem.* **2024**, *180*, 117979. [CrossRef]
26. Sajjan, A.C.; Jha, H.; Borulkar, T.; Regalla, S.; Yadav, R. Systematic Review: Biosensors for Early Detection of Infectious Diseases. *J. Contemp. Clin. Pract.* **2025**, *11*, 195–202. [CrossRef]
27. Noreen, S.; Ishaq, I.; Saleem, M.H.; Muhammad Ali, S.; Iqbal, J. Electrochemical biosensing in oncology: A review advancements and prospects for cancer diagnosis. *Cancer Biol. Ther.* **2025**, *26*, 2475581. [CrossRef]
28. Minta, D.; González, Z.; Menéndez, R.; Gryglewicz, G. Metal-Free Thermally Reduced Graphene Oxide Modified Glassy Carbon Electrode as an Effective Diclofenac Sensor. *Carbon* **2026**, *247*, 120987. [CrossRef]
29. Zhang, C.; Cao, Z.; Zhang, G.; Yan, Y.; Yang, X.; Chang, J.; Song, Y.; Jia, Y.; Pan, P.; Mi, W.; et al. An electrochemical sensor based on plasma-treated zinc oxide nanoflowers for the simultaneous detection of dopamine and diclofenac sodium. *Microchem. J.* **2020**, *158*, 105237. [CrossRef]
30. Boumya, W.; Taoufik, N.; Achak, M.; Bessbousse, H.; Elhalil, A.; Barka, N. Electrochemical sensors and biosensors for the determination of diclofenac in pharmaceutical, biological and water samples. *Talanta Open* **2021**, *3*, 100026. [CrossRef]
31. Kachere, A.R.; Kakade, P.M.; Kanwade, A.R.; Dani, P.; Mandlik, N.T.; Rondiya, S.R.; Dzade, N.Y.; Jadkar, S.R.; Bhosale, S.V. Zinc Oxide/Graphene Oxide Nanocomposites: Synthesis, Characterization and Their Optical Properties. *ES Mater. Manuf.* **2022**, *16*, 19–29. [CrossRef]
32. Alkhuzai, K.A.; Ahmed, A.T.; Ridha, M.; Hannah Jessie Rani, R.; Dash, B.; Al-Hetty, H.R.A.K.; Dariyabi, S.; Vashisht, A.; Hamoodah, Z.J.; Saadi, B.M. Metal Oxides in Drug Detection: Material Innovations in Electrochemical Sensor Development. *J. Chin. Chem. Soc.* **2025**, *72*, 1449–1476. [CrossRef]
33. Jiříčková, A.; Jankovský, O.; Sofer, Z.; Sedmidubský, D. Synthesis and Applications of Graphene Oxide. *Materials* **2022**, *15*, 920. [CrossRef]
34. Măghinici, A.R.; Bounegru, A.V.; Apetrei, C. Electrochemical Detection of Diclofenac Using a Screen-Printed Electrode Modified with Graphene Oxide and Phenanthroline. *Chemosensors* **2025**, *13*, 55. [CrossRef]
35. Kumar, V.; Singh, A.K.; Tiwari, I.; Mishra, L. Novel BN-COOH@ZrO_2/GO Composite for Enhanced Electrical Conductivity and Electrochemical Detection of Diclofenac. *ACS Omega* **2025**, *10*, 1373–1387. [CrossRef]
36. Alamro, F.S.; Medany, S.S.; Al-Kadhi, N.S.; Ahmed, H.A.; Hefnawy, M.A. Modified $NiFe_2O_4$-Supported Graphene Oxide for Effective Urea Electrochemical Oxidation and Water Splitting Applications. *Molecules* **2024**, *29*, 1215. [CrossRef]
37. Chatterjee, S.G.; Chatterjee, S.; Ray, A.K.; Chakraborty, A.K. Graphene–metal oxide nanohybrids for toxic gas sensor: A review. *Sens. Actuators B Chem.* **2015**, *221*, 1170–1181. [CrossRef]
38. Liu, X.; Liu, W.; Ko, M.; Park, M.; Kim, M.G.; Oh, P.; Chae, S.; Park, S.; Casimir, A.; Wu, G.; et al. Metal (Ni, Co)-Metal Oxides/Graphene Nanocomposites as Multifunctional Electrocatalysts. *Adv. Funct. Mater.* **2015**, *25*, 5799–5808. [CrossRef]
39. Khan, M.; Tahir, M.N.; Adil, S.F.; Khan, H.U.; Siddiqui, M.R.H.; Al-warthan, A.A.; Tremel, W. Graphene based metal and metal oxide nanocomposites: Synthesis, properties and their applications. *J. Mater. Chem. A* **2015**, *3*, 18753–18808. [CrossRef]
40. Radić, G.; Šajnović, I.; Petrović, Ž.; Roković, M.K. Reduced Graphene Oxide/α-Fe_2O_3 Fibres as Active Material for Supercapacitor Application. *Croat. Chem. Acta* **2018**, *91*, 481–490. [CrossRef]
41. Putz, H.; Brandenburg, K. Match!—Phase Analysis Using Powder Diffraction. *Cryst. Impact GbR Kreuzherrenstr* **2023**, *102*, 53227.
42. Crystallography Open Database. Open-Access Collection of Crystal Structures of Organic, Inorganic, Metal-Organic Compounds and Minerals, Excluding Biopolymers. Available online: http://www.crystallography.net/cod/ (accessed on 17 August 2024).
43. McCusker, B.L.; Dreele, R.B.; Cox, D.E.; Louer, D.; Scardi, P.J. Rietveld refinement guidelines. *J. Appl. Crystallogr.* **1999**, *32*, 36–50. [CrossRef]
44. Rodrigez-Carvajal, J. *FULLPROF: A Program for Rietveld Refinement and Pattern Matching Analysis*; Abstracts of the Satellite Meeting on Powder Diffraction of the XV Congress of the IUCr; ILL Neutrons for Society: Toulouse, France, 1990; p. 127.
45. Bard, A.J.; Faulkner, L.R. *Electrochemical Methods: Fundamentals and Applications*, 2nd ed.; Wiley: Hoboken, NJ, USA, 2001.
46. de Carvalho, R.C.; Betts, A.J.; Cassidy, J.F. Diclofenac Determination Using CeO_2 Nanoparticle Modified Screen-Printed Electrodes—A Study of Background Correction. *Microchem. J.* **2020**, *158*, 105258. [CrossRef]
47. Anantharaj, S.; Kundu, S. Do the Evaluation Parameters Reflect Intrinsic Activity of Electrocatalysts in Electrochemical Water Splitting? *ACS Energy Lett.* **2019**, *4*, 1260–1264. [CrossRef]
48. Wu, C.; Tang, Y.; Zou, A.; Li, J.; Meng, H.; Gao, F.; Wu, J.; Wang, X. Recommended electrochemical measurement protocol for oxygen evolution reaction. *DeCarbon* **2025**, *8*, 100108. [CrossRef]
49. Wachs, I.E. Number of surface sites and turnover frequencies for oxide catalysts. *J. Catal.* **2022**, *405*, 462–472. [CrossRef]

50. Benedito Da Silva, O.; MacHado, S.A.S. Evaluation of the Detection and Quantification Limits in Electroanalysis Using Two Popular Methods: Application in the Case Study of Paraquat Determination. *Anal. Methods* **2012**, *4*, 2348–2354. [CrossRef]
51. Kresse, G.; Furthmuller, J. Efficient Iterative Schemes for Ab Initio Total-Energy Calculations Using a Plane-Wave Basis Set. *Phys. Rev. B* **1996**, *54*, 11169. [CrossRef]
52. Joubert, D. From Ultrasoft Pseudopotentials to the Projector Augmented-Wave Method. *Phys. Rev. B-Condens. Matter Mater. Phys.* **1999**, *59*, 1758–1775. [CrossRef]
53. Perdew, J.P.; Burke, K.; Ernzerhof, M. Generalized Gradient Approximation Made Simple. *Phys. Rev. Lett.* **1996**, *77*, 3865–3868. [CrossRef]
54. Yang, G.; Li, L.; Lee, W.B.; Ng, M.C. Structure of Graphene and Its Disorders: A Review. *Sci. Technol. Adv. Mater.* **2018**, *19*, 613–648. [CrossRef]
55. Bader, R.F.W. *Atoms in Molecules: A Quantum Theory*; Oxford University Press: Oxford, UK, 1990.
56. Manz, T.A. Introducing DDEC6 Atomic Population Analysis: Part 3. Comprehensive Method to Compute Bond Orders. *RSC Adv.* **2017**, *7*, 45552–45581. [CrossRef]
57. Jauris, I.M.; Matos, C.F.; Saucier, C.; Lima, E.C.; Zarbin, A.J.G.; Fagan, S.B.; Machado, F.M.; Zanella, I. Adsorption of sodium diclofenac on graphene: A combined experimental and theoretical study. *Phys. Chem. Chem. Phys.* **2016**, *18*, 1526–1536. [CrossRef] [PubMed]
58. Yakub, T.; Asthana, A.; Sanwaria, S.; Singh, A.K.; Carabineiro, A.C. Highly Efficient Graphene Oxide/Zinc Oxide/Lignin Catalyst for Photocatalytic Degradation of Methylene Blue and Gentian Violet. *Nanomaterials* **2025**, *15*, 1342. [CrossRef]
59. Tanveer, A.; Arham, S.A. Influence of graphene oxide on the dielectric properties of biogenically synthesized ZnO nanoparticles. *Hybrid Adv.* **2023**, *3*, 100059. [CrossRef]
60. Bingjie, W.; Yiguo, L.; Gengsheng, W.; Zhiqiang, J.; Peng, C.; Zongbao, W.; Qun, G. Reduced graphene oxide enhances the crystallization and orientation of poly(ε-caprolactone). *Compos. Sci. Technol.* **2014**, *96*, 63–70. [CrossRef]
61. Karmakar, K.; Sarkar, A.; Mandal, K.; Khan, G.G. Investigating the Role of Oxygen Vacancies and Lattice Strain Defects on the Enhanced Photoelectrochemical Property of Alkali Metal (Li, Na, and K) Doped ZnO Nanorod Photoanodes. *ChemElectroChem* **2018**, *5*, 1147. [CrossRef]
62. Cuscó, R.; Alarcón-Lladó, E.; Ibáñez, J.; Artús, L.; Jiménez, J.; Wang, B.; Callahan, M.J. Temperature Dependence of Raman Scattering in ZnO. *Phys. Rev. B-Condens. Matter Mater. Phys.* **2007**, *75*, 165202. [CrossRef]
63. Marković, S.; Rajić, V.; Stanković, A.; Veselinović, L.; Belošević-Čavor, J.; Batalović, K.; Abazović, N.; Škapin, S.D.; Uskoković, D. Effect of PEO Molecular Weight on Sunlight Induced Photocatalytic Activity of ZnO/PEO Composites. *Sol. Energy* **2016**, *127*, 124–135. [CrossRef]
64. Lin, K.F.; Cheng, H.M.; Hsu, H.C.; Hsieh, W.F. Band Gap Engineering and Spatial Confinement of Optical Phonon in ZnO Quantum Dots. *Appl. Phys. Lett.* **2006**, *88*, 263117. [CrossRef]
65. Li, Y.; Dai, G.; Zhou, C.; Zhang, Q.; Wan, Q.; Fu, L.; Zhang, J.; Liu, R.; Cao, C.; Pan, A.; et al. Formation and Optical Properties of ZnO:$ZnFe_2O_4$ Superlattice Microwires. *Nano Res.* **2010**, *3*, 326–338. [CrossRef]
66. Jothilakshmi, R.; Ramakrishnan, V.; Thangavel, R.; Kumar, J.; Sarua, A.; Kuball, M. Micro-Raman Scattering Spectroscopy Study of Li-Doped and Undoped ZnO Needle Crystals. *J. Raman Spectrosc.* **2009**, *40*, 556–561. [CrossRef]
67. Boukhoubza, I.; Khenfouch, M.; Achehboune, M.; Leontie, L.; Galca, A.C.; Enculescu, M.; Carlescu, A.; Guerboub, M.; Mothudi, B.M.; Jorio, A.; et al. Graphene Oxide Concentration Effect on the Optoelectronic Properties of ZnO/GO Nanocomposites. *Nanomaterials* **2020**, *10*, 1532. [CrossRef]
68. Azarang, M.; Shuhaimi, A.; Yousefi, R.; Sookhakian, M. Effects of Graphene Oxide Concentration on Optical Properties of ZnO/RGO Nanocomposites and Their Application to Photocurrent Generation. *J. Appl. Phys.* **2014**, *116*, 084307. [CrossRef]
69. Wan, X.; Song, Y.; Zhou, H.; Shao, M. Layered double hydroxides for oxygen evolution reaction towards efficient hydrogen generation. *Energy Mater. Adv.* **2022**, *2022*, 9842610. [CrossRef]
70. Perović, K.; Kovačić, M.; Kraljić Roković, M.; Kušić, H.; Genorio, B.; Lavrenčič Štangar, U.; Lončarić Božić, A. The Development of Ternary-Based TiO_2-SnS_2/GO-RGO Composite Material for Photocatalytic H_2 Production under Solar Light Irradiation. *Mater. Res. Bull.* **2023**, *167*, 112418. [CrossRef]
71. Silva, H.; Mateos-Pedrero, C.; Magén, C.; Pacheco Tanaka, D.A.; Mendes, A. Simple Hydrothermal Synthesis Method for Tailoring the Physicochemical Properties of ZnO: Morphology, Surface Area and Polarity. *RSC Adv.* **2014**, *4*, 31166–31176. [CrossRef]
72. Li, G.R.; Hu, T.; Pan, G.L.; Yan, T.Y.; Gao, X.P.; Zhu, H.Y. Morphology-Function Relationship of ZnO: Polar Planes, Oxygen Vacancies, and Activity. *J. Phys. Chem. C* **2008**, *112*, 11859–11864. [CrossRef]
73. Mclaren, A.; Valdes-Solis, T.; Li, G.; Tsang, S.C. Shape and Size Effects of ZnO Nanocrystals on Photocatalytic Activity. *J. Am. Chem. Soc.* **2009**, *131*, 12540–12541. [CrossRef]
74. Anjana, V.N.; Joseph, M.; Francis, S.; Koshy, E.P.; Mathew, B. ZnO decorated reduced graphene oxide (RGO-ZnO) nanocomposites synthesized via green Benedict's route for efficient water splitting applications and photocatalytic activity. *J. Electroanal. Chem.* **2025**, *998*, 119528. [CrossRef]

75. Ali, F.; Ali, A.; Mooin, G.D.U.; Younas, U.; Nazir, A.; Akyürekli, S.; Iqbal, M.; Mnif, W.; Algarni, Z. Silver and zinc oxide decorated rGO nanocomposites as efficient electrocatalysts towards oxygen evolution reactions under alkaline conditions. *Diam. Relat. Mater.* **2024**, *148*, 111378. [CrossRef]
76. Rostami, M.; Badiei, A.; Rezvaninia, P.; Amiri, A.; Mohammadi Ziarani, G. A Ternary Schottky Heterojunction of RGO/$CuWO_4$/$Ti_3C_2T_x$ in a 2D/0D/2D Nano-Architecture for Dual-Functional Photoelectrochemical Water Splitting and Supercapacitors. *Int. J. Hydrogen Energy* **2026**, *205*, 153309. [CrossRef]
77. Louis, J.; Padmanabhan, N.T.; Jayaraj, M.K.; John, H. Exploring Enhanced Interfacial Charge Separation in ZnO/Reduced Graphene Oxide Hybrids on Alkaline Photoelectrochemical Water Splitting and Photocatalytic Pollutant Degradation. *Mater. Res. Bull.* **2024**, *169*, 112542. [CrossRef]
78. Pataniya, P.M.; Late, D.; Sumesh, C.K. Photosensitive WS_2/ZnO Nano-Heterostructure-Based Electrocatalysts for Hydrogen Evolution Reaction. *ACS Appl. Energy Mater.* **2021**, *4*, 755–762. [CrossRef]
79. Rakočević, L.; Simatović, I.S.; Maksić, A.; Rajić, V.; Štrbac, S.; Srejić, I. Ptau Nanoparticles Supported by Reduced Graphene Oxide as a Highly Active Catalyst for Hydrogen Evolution. *Catalysts* **2022**, *12*, 43. [CrossRef]
80. Aguilar-Lira, G.Y.; Álvarez-Romero, G.A.; Zamora-Suárez, A.; Palomar-Pardavé, M.; Rojas-Hernández, A.; Rodríguez-Ávila, J.A.; Páez-Hernández, M.E. New Insights on Diclofenac Electrochemistry Using Graphite as Working Electrode. *J. Electroanal. Chem.* **2017**, *794*, 182–188. [CrossRef]
81. Dodevska, T.; Shterev, I. Nanomaterials as Catalysts for the Sensitive and Selective Determination of Diclofenac. *ADMET DMPK* **2024**, *12*, 151–165. [CrossRef]
82. Lochab, A.; Baweja, S.; Jindal, K.; Chowdhuri, A.; Tomar, M.; Saxena, R. Experimental and Computational Insights on the Electrochemical Detection of Diclofenac in the Presence of Paracetamol Using Asparagine-Modified MWCNTs. *Microchem. J.* **2025**, *208*, 112430. [CrossRef]
83. Yu, H.; Jiao, J.; Li, Q.; Li, Y. Electrochemical Determination of Diclofenac Sodium in Pharmaceutical Sample Using Copper Nanoparticles/Reduced Graphene Oxide Modified Glassy Carbon Electrode. *Int. J. Electrochem. Sci.* **2021**, *16*, 211024. [CrossRef]
84. Aidli, W.; Comis, S.; Falciola, L.; Pifferi, V. Benzoquinone-Modified Vertically Aligned Mesoporous Silica for Ratiometric Electrochemical Detection of Diclofenac. *Talanta* **2025**, *288*, 127711. [CrossRef]
85. Das, S.; Chakravorty, A.; Luktuke, S.; Raj, A.; Mini, A.A.; Ramesh, K.; Grace, A.N.; Pandey, S.K.; Raghavan, V. Graphene/Gadolinium Oxide Composite Modified Screen-Printed Electrochemical Sensor for Detection of Diclofenac Sodium. *Results Chem.* **2023**, *6*, 101189. [CrossRef]
86. Momma, K.; Izumi, F. VESTA 3 for Three-Dimensional Visualization of Crystal, Volumetric and Morphology Data. *J. Appl. Crystallogr.* **2011**, *44*, 1272–1276. [CrossRef]
87. Wang, V.; Xu, N.; Liu, J.C.; Tang, G.; Geng, W.T. VASPKIT: A User-Friendly Interface Facilitating High-Throughput Computing and Analysis Using VASP Code. *Comput. Phys. Commun.* **2021**, *267*, 108033. [CrossRef]